UNIVERSIDAD NACIONAL AUTÓNOMA DE MÉXICO
PROGRAMA DE DOCTORADO EN INGENIERÍA
Eléctrica – Instrumentación

ERROR ANALYSIS OF STOKES IMAGING POLARIMETERS BASED ON LIQUID CRYSTAL VARIABLE RETARDERS

TESIS
QUE PARA OPTAR POR EL GRADO DE:
DOCTOR EN INGENIERÍA

PRESENTA:

IVÁN MONTES GONZÁLEZ

TUTOR PRINCIPAL:

DR. NEIL CHARLES BRUCE DAVIDSON, ICAT-UNAM

COMITÉ TUTORAL:

DR. MAXIMINO AVENDAÑO ALEJO, ICAT-UNAM

DR. OSCAR G. RODRÍGUEZ HERRERA, ICAT-UNAM

CIUDAD UNIVERSITARIA, CD. MX. Noviembre 2022.

JURADO ASIGNADO:

Presidente: Dr. Qureshi Naser

Secretario: Dr. Cuevas Cardona Salvador C.

1 er. Vocal: Dr. Bruce Davidson Neil Charles

2 do. Vocal: Dr. Avendaño Alejo Maximino

3 er. Vocal: Dr. Rodríguez Herrera Oscar G.

Lugar donde se realizó la tesis: CIUDAD UNIVERSITARIA, CD. MX.

TUTOR DE TESIS:

Dr. Bruce Davidson Neil Charles

“Now I’m in a whole new world with you”

Tabla de Contenido

1 Introduction.. 1

1.1 Structure.. 2

2 Polarimetry.. 4

2.1 Stokes-Mueller formalism.. 6

2.1.1 Stokes parameters.. 6

2.1.2 Mueller matrices.. 10

2.2 Stokes polarimetry.. 14

2.2.1 Polarimetric measurement equation.. 14

2.2.2 Polarimeter optimization.. 16

3 Liquid Crystal Variable Retarders.. 19

3.1 LCVRs operation.. 19

3.2 LCVRs polarimetry... 23

4 Stokes polarimeter.. 27

4.1 Experimental results.. 28

4.2 Calibration method.. 31

5 Stokes imaging polarimeter.. 39

5.1 LCVRs characterization.. 40

5.2 Polarimetric images.. 49

6 Analysis of the effect of experimental errors on the optimization....................... 55

6.1 Individual errors.. 57

6.2 Simultaneous errors... 59

6.3 Optimal alignment... 62

7 Conclusions.. 67

References 69

1 Introduction

The polarization state of light is fundamentally linked to the electric and magnetic field plane of vibration. When light interacts with matter the polarization state is altered, and this change will depend on the physical properties of the material and the incident light. Thus, measuring the polarization allows us to infer more information that can not be obtained directly from irradiance measurements. The complete characterization of the polarization properties of radiation gives important information about the radiation source or its interaction with matter, and plays an important role in many research areas such as remote sensing, medical diagnosis, microscopy, and astronomy [1-8]. For this characterization, Stokes polarimeters are used to determine all the polarization properties of light beams, allowing us to measure the complete Stokes vector of light from irradiance measurements [9,10]. As mentioned in the applications, a partial or full polarization analysis of an extended scene is needed in many situations, in these cases image acquisition is necessary, and imaging polarimetry is used.

Polarimeters based on liquid crystal variable retarders (LCVRs) are widely used [11-16], because of the variable retardance of these devices, allowing manipulation of the polarization state of a light beam. This can be achieved by applying a low voltage, with the benefit of a fast response time and eliminating the errors caused by moving parts. However, due to the nature of the liquid crystals (LC), a well-known problem in these types of devices is that they have spatial variations in the induced retardance. Another problem is the fast axis spatial variations and dependance on the applied voltage. As in all instruments, in addition to systematic errors we also have noise in the irradiance measurements. An optimization is normally used to minimize the noise amplification from the irradiance measurements to the polarimetric information [17-19], but the instrumental errors due to nonideal elements or alignment errors, are not considered in the optimization process. If these errors are not considered, they will lead to polarimetric measurements different from the ideal. Also, a calibration procedure is frequently used to estimate the real values of the component parameters of a polarimeter. However, regardless of the calibration, even if we can accurately estimate the parameters of the polarimeter, the errors can lead to a poorly-optimized instrument, and to a larger than expected noise amplification in the final measurements.

Considering these facts, in this thesis we analyze the effect of the principal errors on Stokes imaging polarimeters based on LCVRs, in order to improve their performance and accuracy. First, we present a description of the capabilities, properties and main problems of LC, which are the main elements of our polarimeter. The real effect and benefits of using an optimization of a Stokes polarimeter is showed. Then, the performance of a calibration method that compensates instrumental errors is verified. For the implementation of an imaging polarimeter, an important factor is that the complete aperture of the LC cell is used. Thus, a characterization method of the induced retardance as a function of the applied voltage, over the full aperture of LCVRs, is proposed. Then, an imaging polarimeter is implemented, to see the real effect of these variations in the polarimetric images. After the experimental results, a numerical analysis of a polarimeter based on two LCVRs is simulated adding errors in the induced retardance and fast-axis orientation, to analyze the effect of these errors in the measurements and in the optimization of imaging polarimeters.

1.1 Structure

In chapter 2 we present a brief description of light and the complete theory used to describe the polarization state of a light beam and the polarizing properties of materials, samples, or polarization components, with the Stokes-Mueller formalism. Then the principles of polarimetry and the main equations are described, as well as the metrics used for the optimization of polarimeters. In chapter 3 we describe the operation and properties of LCVRs, which are used to manipulate the polarization state of light beams, in the polarimeter.

In chapter 4 we present the design and results of an optimized and non-optimized Stokes polarimeter based on two LCVRs. The polarimeter only uses a small part of the LC cell, thus the errors will be smaller, these results are a first approximation to the imaging system. At the end of this chapter a calibration method for Stokes polarimeters is presented and verified using a set of measurements. The calibration method and the obtained results were published as a scientific contribution of this thesis [20].

In chapter 5 we present the characterization of the LCVRs, first measuring the fast-axis orientation as a function of the applied voltage. For the induced retardance characterization, an experimental method to measure the retardance as a function of the applied voltage over the full aperture of a LCVR is presented. The method was used to characterize a pair of variable retarders. This characterization method is another published contribution of this thesis [21]. At the end of this chapter we implement and test a Stokes imaging polarimeter, to see the real effect of these variations. The results show that the nature of the liquid crystals, does not allow us to have as good a system as predicted from the theoretical values. These results were published as a proceedings paper [22].

In chapter 6 we present the numerical simulations of a set of optimized polarimeters, with four measurements, including errors in the induced retardance and fast axis orientation. The analysis is focused on the impact of experimental errors on the optimization. The results will help with the design of Stokes polarimeters based on LCVRs, with lower sensitivity to experimental errors, to help reduce the total error in the final measured Stokes parameters [23]. Chapter 7 summarizes the main conclusions of the work.

2 Polarimetry

Light was described by James Clark Maxwell as an electromagnetic disturbance propagated in the form of waves according to electromagnetic laws. The expressions that describe the behavior of electric and magnetic fields are known as Maxwell's equations [24]. The differential versions of these equations are:

$$\vec{\nabla} \cdot \vec{\mathrm{E}} = \frac{\rho}{\epsilon_0}, \tag{2.0.1}$$

$$\vec{\nabla} \cdot \vec{\mathrm{B}} = 0, \tag{2.0.2}$$

$$\vec{\nabla} x \vec{\mathrm{E}} = -\frac{\partial \vec{\mathrm{B}}}{\partial t}, \tag{2.0.3}$$

$$\vec{\nabla} x \vec{\mathrm{B}} = \mu_0 \vec{\mathrm{J}} + \mu_0 \epsilon_0 \frac{\partial \vec{\mathrm{E}}}{\partial t}, \tag{2.0.4}$$

where $\vec{\mathrm{E}}$ and $\vec{\mathrm{B}}$ represent the electric and magnetic fields, respectively, $\vec{\mathrm{J}}$ represents the current density, μ_0 and ϵ_0 represent the permittivity and permeability of free space and ρ is the electric charge density. Considering equations (2.0.3) and (2.0.4), a time-varying electric field, produced by an accelerated charge, induces a time-dependent magnetic field. This time varying magnetic field will generate an electric field, the process will continue in an endless cycle, moving out from the source as a disturbance through space. This is the electromagnetic phenomenon described by Maxwell that is known as electromagnetic radiation. In free space Maxwell's equations can be manipulated to obtain [24],

$$\nabla^2 \vec{\mathrm{E}} = \mu_0 \epsilon_0 \frac{\partial^2 \vec{\mathrm{E}}}{\partial t^2}, \tag{2.0.5}$$

$$\nabla^2 \vec{\mathrm{B}} = \mu_0 \epsilon_0 \frac{\partial^2 \vec{\mathrm{B}}}{\partial t^2}. \tag{2.0.6}$$

As we can see, these expressions remind us of the differential wave equation with a wave speed of

$$c = \frac{1}{\sqrt{\epsilon_0 \mu_0}} \approx 3x10^8\ m/s. \tag{2.0.7}$$

This is the speed of any electromagnetic wave, in free space. We have seen that light is propagated as a wave with a speed that depends only on the medium, but we have not considered if it is a transverse or longitudinal wave. If we consider a plane wave propagating in the z direction, the electric field is constant in the planes perpendicular to the z direction [24]. This means it is a function only of z and time, therefore, in free space, equation (2.0.1) can be reduced to

$$\frac{\partial E_z}{\partial z} = 0. \tag{2.0.8}$$

This expression has two possibilities, the first one is that E_z is constant for any value of z, but this does not correspond to a traveling wave. The second case is that $E_z = 0$, this corresponds to a wave without an electric field component in the propagation direction, which corresponds to a transverse wave.

Considering the fact that light can be represented as a transverse electromagnetic wave, in order to completely describe the wave, we have to describe the amplitude, frequency and vibration direction of the electric field. The behavior of this vibration direction is referred to as the *polarization* state of the wave. Then, when we talk about *polarimetry*, we are referring to everything related to the measurement and description of the polarization of light.

In this thesis to describe mathematically the polarization state of light beams and the polarization properties of optical elements we use Stokes vectors and Mueller matrices. In the rest of this chapter, we present the description of the Stokes-Mueller formalism. Then the principal relations of polarimetry, in particular the polarimetric equation and the instrument matrix, are described. Finally, two figures of merit used for the optimization of polarimeters are presented.

2.1 Stokes-Mueller formalism

2.1.1 Stokes parameters

The transverse components of the electric field of a beam of light propagating in the z direction, can be represented by two orthogonal wave equations in the x and y directions,

$$\boldsymbol{E_x}(z,t) = E_{0x} cos(\omega t - kz + \delta_x), \tag{2.1.1}$$

$$\boldsymbol{E_y}(z,t) = E_{0y} cos(\omega t - kz + \delta_y), \tag{2.1.2}$$

where δ_x and δ_y are the phases, E_{0x} and E_{0y} are the amplitudes of the components in the x and y directions, respectively. The parameter ω is the angular frequency of the light wave, and k is the wave number, $k = 2\pi/\lambda$, with λ the wavelength of the light. Following the procedure presented by Goldstein [9], we can obtain the equation:

$$\frac{E_x^2}{E_{0x}^2} + \frac{E_y^2}{E_{0y}^2} - 2\frac{E_x}{E_{0x}}\frac{E_y}{E_{0y}} \cos\delta = \sin^2\delta. \tag{2.1.3}$$

Equation (2.1.3) describes the polarization ellipse, which shows the complete behavior described by the electric field. In Fig. 2.1.1, we show the plot of the polarization ellipse.

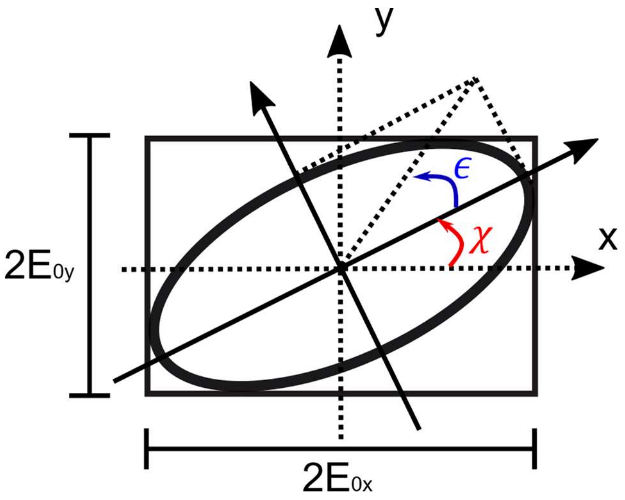

Fig. 2.1.1 Representation of the polarization ellipse.

The azimuth angle of the polarization ellipse, χ (0°<χ<180°), is related to the parameters E_{0x}, E_{0y} and δ as:

$$\tan 2\chi = \frac{2E_{0x}E_{0y}}{E_{0x}^2 - E_{0y}^2}\cos\delta. \tag{2.1.4}$$

The ellipticity, ϵ (-45°<ϵ<45°), is the ratio of the semi-major axis to the semi-minor axis of the polarization ellipse and is related to the parameters E_{0x}, E_{0y}, and δ as:

$$\sin 2\epsilon = \frac{2E_{0x}E_{0y}}{E_{0x}^2 + E_{0y}^2}\sin\delta. \tag{2.1.5}$$

We can define the Stokes parameters, for any polarization of the beam of light, in terms of elements of the polarization ellipse as follows [9]:

$$S_0 = E_{0x}^2 + E_{0y}^2,\ S_1 = E_{0x}^2 - E_{0y}^2,\ S_2 = 2E_{0x}E_{oy}\cos\delta\ ,\ S_3 = 2E_{0x}E_{oy}\sin\delta. \tag{2.1.6}$$

It is important to comment that the light beam can be either completely or partially polarized, and it can be shown [9] that:

$$S_0^2 \geq S_1^2 + S_2^2 + S_3^2. \tag{2.1.7}$$

The equality is satisfied when the light beam is completely polarized, and the inequality when the light is partially polarized. In the case of unpolarized light $S_1 = S_2 = S_3 = 0$.

The terms of equation (2.1.6) can be arranged in a column vector that is called the Stokes vector, expressed as [9]

$$\boldsymbol{S} = \begin{pmatrix} S_0 \\ S_1 \\ S_2 \\ S_3 \end{pmatrix} = \begin{pmatrix} E_{0x}^2 + E_{0y}^2 \\ E_{0x}^2 - E_{0y}^2 \\ 2E_{0x}E_{oy}\cos\delta \\ 2E_{0x}E_{oy}\sin\delta \end{pmatrix}. \tag{2.1.8}$$

The Stokes vector as a function of the ellipticity and azimuth angle, with a total irradiance I_0, can be expressed as

$$\boldsymbol{S} = \begin{pmatrix} S_0 \\ S_1 \\ S_2 \\ S_3 \end{pmatrix} = I_0 \begin{pmatrix} 1 \\ \cos(2\epsilon)\cos(2\chi) \\ \cos(2\epsilon)\sin(2\chi) \\ \sin(2\epsilon) \end{pmatrix}. \tag{2.1.9}$$

Furthermore, the four parameters are real values and are related to irradiance measurements. The first parameter, S_0, is the total irradiance of the light beam. While the other 3 parameters represent the amount of a polarization component contained in the light beam. We can rewrite the Stokes parameters in terms of the irradiance polarization components as [9],

$$\boldsymbol{S} = \begin{pmatrix} S_0 \\ S_1 \\ S_2 \\ S_3 \end{pmatrix} = \begin{pmatrix} I_0 = I_h + I_v = I_{+4} \;\; + I_{-4} \;\; = I_{cr} + I_{cl} \\ I_h - I_v \\ I_{+45} - I_{-45} \\ I_{cr} - I_{cl} \end{pmatrix}, \tag{2.1.10}$$

where I is the irradiance measurement of a given polarization component, the subscripts $h, v, +45, -45$, represent the linear horizontal, vertical, at +45°, and at -45°, polarization component, respectively. The other two subscripts, cr and cl, represent the circular right and left polarization components.

When describing the polarization state of a light beam, the Degree Of Polarization (DOP), the ellipticity, and the azimuth angle of the polarization ellipse, are important quantities that can be directly calculated using the Stokes parameters. In other words, we can calculate them using irradiance measurements. The DOP is defined as [9],

$$DOP = \frac{P_{pol}}{P_{total}} = \frac{\sqrt{S_1^2 + S_2^2 + S_3^2}}{S_0}, \;\; 0 \leq DOP \leq 1. \tag{2.1.11}$$

The value 0 is obtained when the light beam is unpolarized and 1 when the beam is completely polarized. The ellipticity and azimuth angle are calculated using the relationships:

$$\epsilon = \frac{1}{2}\arcsin\left(\frac{S_3}{S_0}\right), \;\; \chi = \frac{1}{2}\arctan\left(\frac{S_2}{S_1}\right). \tag{2.1.12}$$

The Stokes parameters, the ellipticity and the azimuth angle of the polarization ellipse were used by Poincaré, to establish a model to represent the polarization state of a light beam in a sphere, as shown in Fig. 2.1.2. Every point P on the sphere represents a unique polarization state and the parameters S_1, S_2 and S_3 are the Cartesian coordinates of the point P, on the sphere of radius S_0.

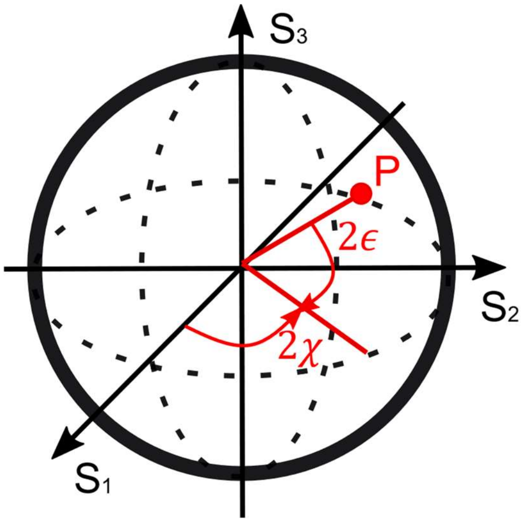

Fig. 2.1.2 Representation of the Poincaré sphere.

Then every point in the Poincaré sphere represents a Stokes vector. For example, unpolarized light is represented in the center of the sphere, where $S_1 = S_2 = S_3 = 0$, and the Stokes vector is

$$\boldsymbol{S} = \begin{pmatrix} S_0 \\ 0 \\ 0 \\ 0 \end{pmatrix}. \tag{2.1.13}$$

If the point is on the surface of the sphere, it represents a fully polarized state. For example, for linear polarizations where the ellipticity is $\epsilon = 0$, the value of S_3 will always be 0 and can be represented on the equator of the Poincaré sphere. The Stokes vector of linearly polarized light can be described as

$$\boldsymbol{S} = \begin{pmatrix} S_0 \\ S_1 \\ S_2 \\ S_3 \end{pmatrix} = I_0 \begin{pmatrix} 1 \\ \cos(2\chi) \\ \sin(2\chi) \\ 0 \end{pmatrix}. \tag{2.1.14}$$

Circular polarized light, where the ellipticity is $\epsilon = +45°$ for circular right (cr) and $\epsilon = -45°$ for circular left (cl), are represented on the north and south poles, respectively, of the Poincaré sphere. Any other value of ϵ, or latitude in the Poincaré sphere, is referred to as elliptical polarization. The Stokes vectors for various polarizations are shown in table 2.1.1.

$\chi = 0°$ or $\chi = 90°$ $\epsilon = 0°$	$\chi = \pm 45°$ $\epsilon = 0°$	$\chi = \pm 22.5°$ $\epsilon = 0°$	$\epsilon = \pm 45°$	$\chi = 22.5°$ $\epsilon = 17.6°$
$I_0\begin{pmatrix}1\\\pm1\\0\\0\end{pmatrix}$	$I_0\begin{pmatrix}1\\0\\\pm1\\0\end{pmatrix}$	$I_0\begin{pmatrix}1\\1/\sqrt{2}\\\pm1/\sqrt{2}\\0\end{pmatrix}$	$I_0\begin{pmatrix}1\\0\\0\\\pm1\end{pmatrix}$	$I_0\begin{pmatrix}1\\0.577\\0.577\\0.577\end{pmatrix}$

Table 2.1.1. Stokes vectors of polarized beams.

2.1.2 Mueller matrices

We have seen that the polarization properties of a light beam can be described by a Stokes vector. If the beam interacts with a polarizing element, after emerging it is described by a new Stokes vector. Fig. 2.1.3 shows a representation of an incident beam interacting with a polarizing element or system.

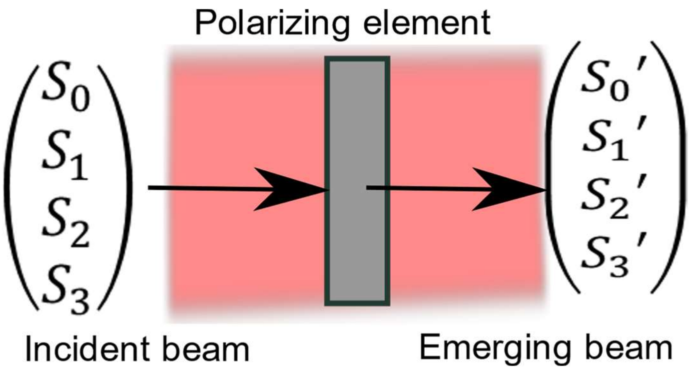

Fig. 2.1.3. Light beam through a polarizing element.

The new Stokes vector can be expressed as a linear combination of the incident Stokes parameters. Particularly we can represent a linear combination as a matrix, then

$$\begin{pmatrix} S_0' \\ S_1' \\ S_2' \\ S_3' \end{pmatrix} = \begin{pmatrix} m_{00} & m_{01} & m_{02} & m_{03} \\ m_{10} & m_{11} & m_{12} & m_{13} \\ m_{20} & m_{21} & m_{22} & m_{23} \\ m_{30} & m_{31} & m_{32} & m_{33} \end{pmatrix} \begin{pmatrix} S_0 \\ S_1 \\ S_2 \\ S_3 \end{pmatrix}, \tag{2.1.15}$$

or

$$\boldsymbol{S}' = \bar{\boldsymbol{M}}\boldsymbol{S}, \tag{2.1.16}$$

where $\boldsymbol{S}$ is the Stokes vector of the incident beam, and $\boldsymbol{S}'$ is the Stokes vector of the emerging beam. The matrix $\bar{\boldsymbol{M}}$ is a 4×4 real matrix, called the Mueller matrix, and has the complete information of the polarization properties of any surface, optical system or medium. In other words, for an incident light beam with an arbitrary polarization state, if we know the Mueller matrix of the medium, we can calculate the polarization state of the light beam emerging from the medium.

The two main polarizing elements used in practice are linear polarizers and retarders. A polarizer is an element that unequally changes the amplitudes of the orthogonal components of the incident beam. An ideal linear polarizer has a fixed transmission axis, where the parallel component of the beam will be completely transmitted, and the amplitude in the orthogonal direction will be completely absorbed. The Mueller matrix of an ideal linear polarizer with its transmission axis at an angle θ is,

$$\bar{\boldsymbol{M}}_P(\theta) = \frac{1}{2}\begin{pmatrix} 1 & \cos(2\theta) & \sin(2\theta) & 0 \\ \cos(2\theta) & \cos^2(2\theta) & \sin(2\theta)\cos(2\theta) & 0 \\ \sin(2\theta) & \sin(2\theta)\cos(2\theta) & \sin^2(2\theta) & 0 \\ 0 & 0 & 0 & 0 \end{pmatrix}. \tag{2.1.17}$$

An important property of linear polarizers is that the emerging beam will always be linearly polarized, independently of the incident polarization. This can be seen in the following calculation

$$\boldsymbol{S}' = \frac{1}{2}\begin{pmatrix} 1 & \cos(2\theta) & \sin(2\theta) & 0 \\ \cos(2\theta) & \cos^2(2\theta) & \sin(2\theta)\cos(2\theta) & 0 \\ \sin(2\theta) & \sin(2\theta)\cos(2\theta) & \sin^2(2\theta) & 0 \\ 0 & 0 & 0 & 0 \end{pmatrix}\begin{pmatrix} S_0 \\ S_1 \\ S_2 \\ S_3 \end{pmatrix}, \quad (2.1.18a)$$

$$\boldsymbol{S}' = \frac{1}{2}(S_0 + \cos(2\theta)\,S_1 + \sin(2\theta)\,S_2)\begin{pmatrix} 1 \\ \cos(2\theta) \\ \sin(2\theta) \\ 0 \end{pmatrix}. \quad (2.1.18b)$$

The emerging Stokes vector has the form of equation (2.1.14), which represents linearly polarized light with azimuth angle aligned with the transmission axis of the polarizer, θ.

A retarder is an element that introduces a phase shift of δ between orthogonal components of the incident light, caused by the birefringence of the material. The birefringence is the characteristic of some materials to possess two different refractive indices. Because of the difference in the refractive index, the two components travel at different speeds inside the element, producing the phase shift. The birefringence is defined as,

$$\Delta n = |n_e - n_o|, \quad (2.1.19)$$

where n_e is the extraordinary refractive index, and n_o is the ordinary refraction index. The phase shift produced by the birefringence is also called retardance and is defined as,

$$\delta = \frac{2\pi}{\lambda} d\Delta n, \quad (2.1.20)$$

where λ is the wavelength of the incident beam and d is the width of the retarder. The principal axes of a retarder are referred to as the fast and the slow axes, related to the ordinary and extraordinary refractive indices. The Mueller matrix of a retarder with fast axis at θ and a retardance δ is

$$\overline{\boldsymbol{M}}_R(\delta,\theta) = \begin{pmatrix} 1 & 0 & 0 & 0 \\ 0 & \cos^2(2\theta) + \cos(\delta)\sin^2(2\theta) & \big(1-\cos(\delta)\big)\sin(2\theta)\cos(2\theta) & -\sin(\delta)\sin(2\theta) \\ 0 & \big(1-\cos(\delta)\big)\sin(2\theta)\cos(2\theta) & \sin^2(2\theta) + \cos(\delta)\cos^2(2\theta) & \sin(\delta)\cos(2\theta) \\ 0 & \sin(\delta)\sin(2\theta) & -\sin(\delta)\cos(2\theta) & \cos(\delta) \end{pmatrix}.$$

(2.1.21)

In retarders if the incident light is unpolarized then the emerging beam will still be unpolarized, so they have an effect only when using polarized light. The Mueller matrices of a pair of retarders with a variable phase shift at two fixed orientations are shown in table 2.1.2

$\theta = 0°$	$\theta = 45°$
$\begin{pmatrix} 1 & 0 & 0 & 0 \\ 0 & 1 & 0 & 0 \\ 0 & 0 & \cos(\delta) & \sin(\delta) \\ 0 & 0 & -\sin(\delta) & \cos(\delta) \end{pmatrix} \begin{pmatrix} S_0 \\ S_1 \\ S_2 \\ S_3 \end{pmatrix} = \begin{pmatrix} S_0 \\ S_1 \\ S_2\cos(\delta) + S_3\sin(\delta) \\ -S_2\sin(\delta) + S_3\cos(\delta) \end{pmatrix}$	$\begin{pmatrix} 1 & 0 & 0 & 0 \\ 0 & \cos(\delta) & 0 & -\sin(\delta) \\ 0 & 0 & 1 & 0 \\ 0 & \sin(\delta) & 0 & \cos(\delta) \end{pmatrix} \begin{pmatrix} S_0 \\ S_1 \\ S_2 \\ S_3 \end{pmatrix} = \begin{pmatrix} S_0 \\ S_1\cos(\delta) - S_3\sin(\delta) \\ S_2 \\ S_1\sin(\delta) + S_3\cos(\delta) \end{pmatrix}$

Table 2.1.2. Mueller matrices and the emerging Stokes vectors, from retarders at a predefined orientation.

The Mueller matrices of a pair of retarders with a fixed phase shift are shown in table 2.1.3.

$\delta = 90°$ Quarter-wave plate	$\delta = 180°$ Half-wave plate
$\begin{pmatrix} 1 & 0 & 0 & 0 \\ 0 & \cos^2(2\theta) & \sin(2\theta)\cos(2\theta) & -\sin(2\theta) \\ 0 & \sin(2\theta)\cos(2\theta) & \sin^2(2\theta) & \cos(2\theta) \\ 0 & \sin(2\theta) & -\cos(2\theta) & 0 \end{pmatrix} \begin{pmatrix} S_0 \\ S_1 \\ S_2 \\ S_3 \end{pmatrix} = \begin{pmatrix} S_0 \\ \cos^2(2\theta)S_1 + \sin(2\theta)\cos(2\theta)S_2 - \sin(2\theta)S_3 \\ \sin(2\theta)\cos(2\theta)S_1 + \sin^2(2\theta)S_2 + \cos(2\theta)S_3 \\ \sin(2\theta)S_1 - \cos(2\theta)S_2 \end{pmatrix}$	$\begin{pmatrix} 1 & 0 & 0 & 0 \\ 0 & \cos(4\theta) & \sin(4\theta) & 0 \\ 0 & \sin(4\theta) & -\cos(4\theta) & 0 \\ 0 & 0 & 0 & -1 \end{pmatrix} \begin{pmatrix} S_0 \\ S_1 \\ S_2 \\ S_3 \end{pmatrix} = \begin{pmatrix} S_0 \\ \cos(4\theta)S_1 - \sin(4\theta)S_2 \\ \sin(4\theta)S_1 - \cos(4\theta)S_2 \\ 0 - S_3 \end{pmatrix}$

Table 2.1.3. Mueller matrices Mueller matrices and the emerging Stokes vectors, from retarders with predefined retardance.

It is important to mention that the Mueller matrix of an optical system, based on various polarizing elements, can be described by the right to left product of the Mueller matrices individually,

$$\bar{\boldsymbol{M}}_{\boldsymbol{sys}} = \bar{\boldsymbol{M}}_{\boldsymbol{i}} \dots \bar{\boldsymbol{M}}_{\boldsymbol{2}} \bar{\boldsymbol{M}}_{\boldsymbol{1}}, \tag{2.1.22}$$

where the subscript i represents the i-th element of the complete optical system.

2.2 Stokes polarimetry

In equation (2.1.10) we define the Stokes parameters in an irradiance formulation, so we can measure them. A Stokes polarimeter allows us to determine some or all the four Stokes parameters, that is the partial or the complete Stokes vector of a light beam. For a complete Stokes polarimeter the six ideal measurements shown in equation (2.1.10) are not the only way to measure the Stokes vector, we can use different sets of measurements to reconstruct the Stokes parameters. In this section we present the formulation of the procedure to measure the Stokes parameters, and two metrics commonly used in the optimization process of polarimeters.

2.2.1 Polarimetric measurement equation

The light beam to be analyzed passes through a Polarization State Analyzer (PSA). We refer to a PSA as all the polarization elements used to measure the polarization state of an incident beam. The Stokes parameters are determined by a set of irradiance measurements for different configurations of the PSA, each configuration measures the irradiance of a different polarization component of the incident beam. Above we provide the relation between an input and output Stokes vector, which is written in terms of the Mueller matrix of the optical system:

$$\begin{pmatrix} S_0{}' \\ S_1{}' \\ S_2{}' \\ S_3{}' \end{pmatrix} = \begin{pmatrix} m_{00} & m_{01} & m_{02} & m_{03} \\ m_{10} & m_{11} & m_{12} & m_{13} \\ m_{20} & m_{21} & m_{22} & m_{23} \\ m_{30} & m_{31} & m_{32} & m_{33} \end{pmatrix} \begin{pmatrix} S_0^{inc} \\ S_1^{inc} \\ S_2^{inc} \\ S_3^{inc} \end{pmatrix}. \tag{2.1.15}$$

In this case we measure the irradiance of the output beam, which is given by the component $S_0{}'$ of the output Stokes vector, and:

$$I = S_0' = (m_{00} \quad m_{01} \quad m_{02} \quad m_{03}) \begin{pmatrix} S_0^{inc} \\ S_1^{inc} \\ S_2^{inc} \\ S_3^{inc} \end{pmatrix} = (m_{00} \quad m_{01} \quad m_{02} \quad m_{03}) \boldsymbol{S}^{inc}. \quad (2.2.1)$$

The measured irradiances for the different polarimeter configurations can be organized into a vector $\boldsymbol{I}$, which is related to the unknown input Stokes vector $\boldsymbol{S}^{in}$ by the polarimetric measurement equation [10]

$$\boldsymbol{I} = \overline{\boldsymbol{A}} \boldsymbol{S}^{inc}, \quad (2.2.2)$$

where $\overline{\boldsymbol{A}}$ is a $[Nx4]$ real, non-singular matrix, N represents the number of measurements, or configurations of the polarimeter. This matrix is called the instrument matrix and can be defined as

$$\overline{\boldsymbol{A}} = \begin{pmatrix} \left(\overline{\boldsymbol{M}}_{PSA(1)}\right)_{\boldsymbol{1}} \\ \left(\overline{\boldsymbol{M}}_{PSA(2)}\right)_{\boldsymbol{1}} \\ \vdots \\ \left(\overline{\boldsymbol{M}}_{PSA(N)}\right)_{\boldsymbol{1}} \end{pmatrix}, \quad (2.2.3)$$

where $\overline{\boldsymbol{M}}_{PSA(N)}$ is the Mueller matrix of the PSA in the N-th configuration of the polarimeter, and the subscript 1 represents the first row of each Mueller matrix. The irradiance measurements are the linear combinations of the incident Stokes parameters,

$$\begin{pmatrix} I_1 \\ I_2 \\ \vdots \\ I_N \end{pmatrix} = \begin{pmatrix} a_{10} & a_{11} & a_{12} & a_{13} \\ a_{20} & a_{21} & a_{22} & a_{23} \\ \vdots & \vdots & \vdots & \vdots \\ a_{N0} & a_{N1} & a_{N2} & a_{N3} \end{pmatrix} \begin{pmatrix} S_0^{inc} \\ S_1^{inc} \\ S_2^{inc} \\ S_3^{inc} \end{pmatrix}. \quad (2.2.4)$$

It is important to mention that the instrument matrix does not represent a Mueller matrix, in this matrix each row is the first row of the Mueller matrix for different configurations of the optical systems. Each measurement can be expressed as,

$$I_N = a_{N0} S_0^{inc} + a_{N1} S_1^{inc} + a_{N2} S_2^{inc} + a_{N3} S_3^{inc}. \quad (2.2.5)$$

Each measurement represents the irradiance of a given polarization state analyzed, which can also be represented as a Stokes vector. To determine the complete unknown input Stokes vector, an inversion process of the instrument matrix is necessary. A condition of the instrument matrix is that should be invertible, and then we have two cases. First, when $N = 4$, where $\bar{\boldsymbol{A}}^{-\mathbf{1}}$ exists and is unique, the data reduction equation is then

$$\boldsymbol{S}^{in} = \bar{\boldsymbol{A}}^{-\mathbf{1}}\boldsymbol{I}. \tag{2.2.6}$$

The second case is when $N > 4$. $\bar{\boldsymbol{A}}$ is a rectangular matrix, the system is overdetermined and $\bar{\boldsymbol{A}}^{-\mathbf{1}}$ is not unique. A solution that minimizes the mean square error can be obtained by using the Moore-Penrose pseudoinverse, leading to the following equation to obtain the input Stokes vector:

$$\boldsymbol{S}^{in} = (\bar{\boldsymbol{A}}^{\boldsymbol{T}}\,\bar{\boldsymbol{A}})^{-\mathbf{1}}\bar{\boldsymbol{A}}^{\boldsymbol{T}}\,\boldsymbol{I} = \bar{\boldsymbol{A}}^{\boldsymbol{p}}\,\boldsymbol{I}, \tag{2.2.7}$$

$\bar{\boldsymbol{A}}^{\boldsymbol{p}}$ denotes the Moore-Penrose pseudoinverse of $\bar{\boldsymbol{A}}$.

2.2.2 Polarimeter optimization

When measuring the Stokes parameters we normally have noise in the irradiance measurements, and different instrument matrices will lead to different transmission of the noise to the measured Stokes parameters. To maximize the signal to noise ratio, the optimization of the instrument matrix, $\bar{\boldsymbol{A}}$, is often related to its singular value decomposition [18,25]. The singular value decomposition permits us to factorize the instrument matrix in the form [26],

$$\bar{\boldsymbol{A}} = \bar{\boldsymbol{U}}\bar{\boldsymbol{D}}\bar{\boldsymbol{V}}^{\boldsymbol{T}} = [\boldsymbol{u}_{\mathbf{1}}\,\boldsymbol{u}_{\mathbf{2}}\dots\boldsymbol{u}_{\boldsymbol{N}}]\begin{pmatrix} \sigma_1 & \mathbf{0} & \mathbf{0} & \mathbf{0} \\ \mathbf{0} & \sigma_2 & \mathbf{0} & \mathbf{0} \\ \mathbf{0} & \mathbf{0} & \sigma_3 & \mathbf{0} \\ \mathbf{0} & \mathbf{0} & \mathbf{0} & \sigma_4 \\ \vdots & \vdots & \vdots & \vdots \end{pmatrix}[\boldsymbol{v}_{\mathbf{1}}\,\boldsymbol{v}_{\mathbf{2}}\dots\boldsymbol{v}_{\mathbf{4}}]^{\boldsymbol{T}}, \tag{2.2.8}$$

where $\bar{\boldsymbol{U}}$ consists of N orthonormalized eigenvectors of $\bar{\boldsymbol{A}}\bar{\boldsymbol{A}}^{\boldsymbol{T}}$ and the matrix $\bar{\boldsymbol{V}}$ consists of the orthonormalized eigenvectors of $\bar{\boldsymbol{A}}^{\boldsymbol{T}}\bar{\boldsymbol{A}}$. σ_j are the non-zero singular values, the number of singular values is related to the rank of the instrument matrix.

For a full Stokes polarimeter, the rank of the matrix $\overline{\boldsymbol{A}}$ is $R = 4$, for an incomplete polarimeter $R < 4$. Tyo [18] showed that to reduce the effect of noise in the measurements on the final solution, the instrument matrix must be optimized, by reducing its condition number (CN), which is related to the singular values. The CN is defined as the product of the norm of the matrix and the norm of its inverse:

$$\kappa(\overline{\boldsymbol{A}}) = \|\overline{\boldsymbol{A}}\|\left\|\overline{\boldsymbol{A}}^{-\mathbf{1}}\right\|. \tag{2.2.9}$$

In terms of the singular values, we have

$$\|\overline{\boldsymbol{A}}\| = \sigma_1, \ \left\|\overline{\boldsymbol{A}}^{-\mathbf{1}}\right\| = \frac{1}{\sigma_j}, \tag{2.2.10}$$

where σ_1 is the largest singular value and σ_j is the smallest nonzero singular value. Then we can define the CN as the ratio of the largest to the smallest singular value of $\overline{\boldsymbol{A}}$. Therefore, reducing the condition number is equivalent to equate the range of the singular values, maximizing the relative importance of each measurement. With the minimum CN we also ensure that we have a matrix as far from singular as possible, since if the matrix is singular the condition number is infinite. In the presence of noise in the irradiance measurements we can rewrite the polarimetric equation (2.2.2) as,

$$(\boldsymbol{I} + \delta\boldsymbol{I}) = \overline{\boldsymbol{A}}\left(\boldsymbol{S}^{in} + \delta\boldsymbol{S}^{in}\right), \tag{2.2.11}$$

where $\boldsymbol{\delta I}$ represents the error in the irradiance measurements and $\boldsymbol{\delta S}^{in}$ the error in the Stokes vector measured. Consequently, we can obtain the following equation [27],

$$\frac{\|\overline{\boldsymbol{\delta S}^{in}}\|}{\|\overline{\boldsymbol{S}}^{in}\|} \leq \kappa(\overline{\boldsymbol{A}}) \frac{\|\delta\overline{\boldsymbol{I}}\|}{\|\overline{\boldsymbol{I}}\|}. \tag{2.2.12}$$

Minimizing the CN of the instrument matrix minimizes the noise in the Stokes vector measured. In the literature. It has been shown that the minimum condition number for a Stokes polarimeter is $\sqrt{3}$, independently of the number of measurements made with the polarimeter[18]. Another figure of merit often used is the equally weighted variance (EWV) which is defined as [25],

$$EWV = \sum_{j=1}^{R} 1/\,\sigma_j^2, \tag{2.2.13}$$

where R is the rank of the instrument matrix, and σ_j are all the singular values. A benefit of the EWV is that it weights all the singular values equally. As we can see the singular values are in the denominator, then the EWV diverges when the instrument matrix is close to singular. To optimize a polarimeter the EWV should be minimized. Foreman et. al. [28], showed that the minimum $EWV = 40/N$, showing that increasing number of measurements reduces the noise amplification.

The EWV, unlike the CN, detects the benefits of increasing the number of measurements. Due to the use of a ratio of the singular values in the CN, the effect of any change to the system which scales the singular values together is cancelled out, which is the reason that the number of measurements has no effect on the CN. Considering this fact, the EWV is recommended in the case of redundant measurements.

Goudail and Foreman [19], showed that the optimization of polarimeters using the EWV or CN led to the same optimal set of measurements. The set of measurements in the polarimeter can be represented by N unmatched points in the Poincaré sphere. Both figures of merit lead to a maximum volume spherical N design, known as Platonic solids. For example, for $N = 4$ we obtain a regular tetrahedron, and for $N = 6$ an octahedron. Then the optimization of polarimeters reduces to maximizing the volume of these platonic solids in the Poincaré sphere.

3 Liquid Crystal Variable Retarders

As mentioned before, a Stokes polarimeter is a device that estimates the four Stokes parameters containing all the polarization information. This is achieved by measuring the irradiance of at least four adequate polarization components. With a set of different irradiance measurements, we can reconstruct the Stokes vector as shown in section 2.2.1. To measure different polarization components, the polarimeter requires a control in the polarization state of the incident beam. In this thesis we decided to use LCVRs to manipulate the polarization state of a light beam. The advantage of using these devices is the capability of reorienting the liquid-crystal molecules with an external applied voltage. This reorientation changes the induced retardance thus the polarization can be modulated, making them very useful to analyze the polarization state of light. In this chapter we present the description of the nature of liquid crystals, their main properties and their function as variable retarders in a polarimeter.

3.1 LCVR operation

The way that molecules interact with each other determines the phases of matter, like solids, liquids, gases, or liquid crystals. In solids, the molecules have fixed positions and are held together by very strong intermolecular forces. They have definite shape and volume, but they can vibrate. In the case of crystalline solids, the molecules that compose the solid have a well-defined arrangement in a definite pattern, with internal symmetry. This long-range order means that once the position of a molecule and the molecules beside it are known at some point, the positions of the other molecules throughout the crystal are also known. Also, the position and orientation of molecules are correlated. Uniaxial crystals are anisotropic materials, so they have different physical properties in different directions. In liquids, the molecules have enough space between them, so they can move around. Although molecules are not fixed in one position, they are also subject to intermolecular attraction that maintains the volume constant, but not the shape. Liquids have short range order where nearby molecules have an order but at some distance, the position and orientation of the molecules are uncorrelated.

Liquid crystal is a mesophase of matter that has properties between a solid and a liquid, materials in this mesophase have a combination of long-range order and mobility. In liquid crystals the correlation of position is lost, and molecules can move as in liquids, but the orientation correlation is maintained as in a crystal. In this thesis we use nematic liquid crystals, these are formed by long molecules, with a large dipole moment, that tend to be aligned without any positional order. The prevailing orientation of the liquid crystal molecules is called the director. In Fig. 3.1.1, we show a representation of three states of matter. From left to right first we represent a crystalline solid, where molecules cannot move in x-y-x or change orientation, they can only vibrate. Then a nematic liquid crystal where molecules have a preferential orientation, but they can move in x-y-z freely. Finally, a liquid where molecules can move around and change orientation.

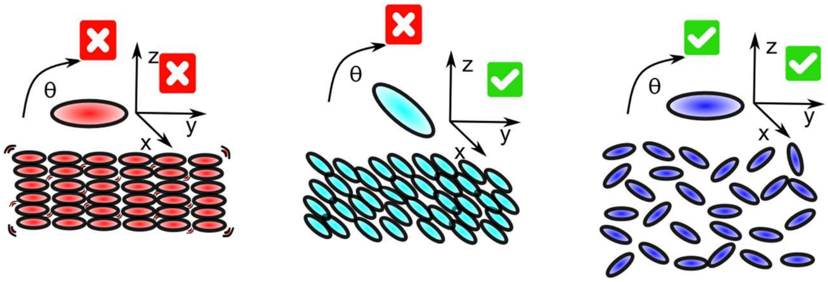

Fig. 3.1.1 Molecules in a solid, a nematic liquid crystal and a liquid.

The nematic liquid crystals exhibit optical anisotropy or birefringence, meaning that they possess two different refractive indices, as a result of the long shape of the molecules. When an electromagnetic wave goes through a liquid crystal, the part of the electric field that oscillates parallel to the director gets slowed down more than the perpendicular part. The parallel component experiences an extraordinary refractive index, n_e , while the perpendicular component experiences the ordinary refractive index, n_o. This behavior is represented in Fig. 3.1.2, where $\boldsymbol{E_x}$ and $\boldsymbol{E_y}$ are the polarization components represented in equations 2.1.1 and 2.1.2. $\boldsymbol{k}$ is the direction of propagation of light.

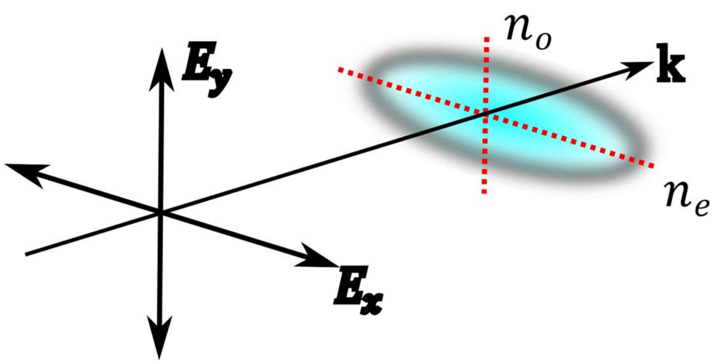

Fig. 3.1.2 Ordinary and extraordinary refractive index in nematic liquid crystal molecule.

If light passes through a cell filled with a nematic liquid crystal, the parallel and perpendicular components travel at different speeds producing a phase shift between components. If the optical axis or director is perpendicular to the light propagation, they will have the same effect as a retarder with slow or fast axis along the director, and retardance δ. As seen in the previous chapter, this element can be described by the Mueller matrix:

$$\overline{\boldsymbol{M}}_R(\delta,\theta) = \begin{pmatrix} 1 & 0 & 0 & 0 \\ 0 & \cos^2(2\theta)+\cos(\delta)\sin^2(2\theta) & \big(1-\cos(\delta)\big)\sin(2\theta)\cos(2\theta) & -\sin(\delta)\sin(2\theta) \\ 0 & \big(1-\cos(\delta)\big)\sin(2\theta)\cos(2\theta) & \sin^2(2\theta)+\cos(\delta)\cos^2(2\theta) & \sin(\delta)\cos(2\theta) \\ 0 & \sin(\delta)\sin(2\theta) & -\sin(\delta)\cos(2\theta) & \cos(\delta) \end{pmatrix}. \tag{2.1.21}$$

Liquid crystal cells or LCVRs are usually made with a transparent cell with an alignment layer, filled with a nematic liquid crystal. The alignment layer is used to determine the director of the molecules. To have control of the polarization, LCVRs use a conductive layer to apply an electric field that alters the molecule, reorienting them and changing the induced retardance, this reorientation is possible due to the large dipolar moment of the molecules. When an electric field is applied the reorientation produces a change in the molecule symmetry, and the extraordinary refractive index changes, therefore, it is possible to manipulate the induced retardance. This effect is represented in Fig. 3.1.3., where the applied voltages are represented as $V_1 = 0V < V_2 < V_3 < V_4 < V_5 < V_6 < V_7$. Without any applied voltage the retardance is maximum. When a voltage is applied the molecules reorientate and the induced retardance is lower.

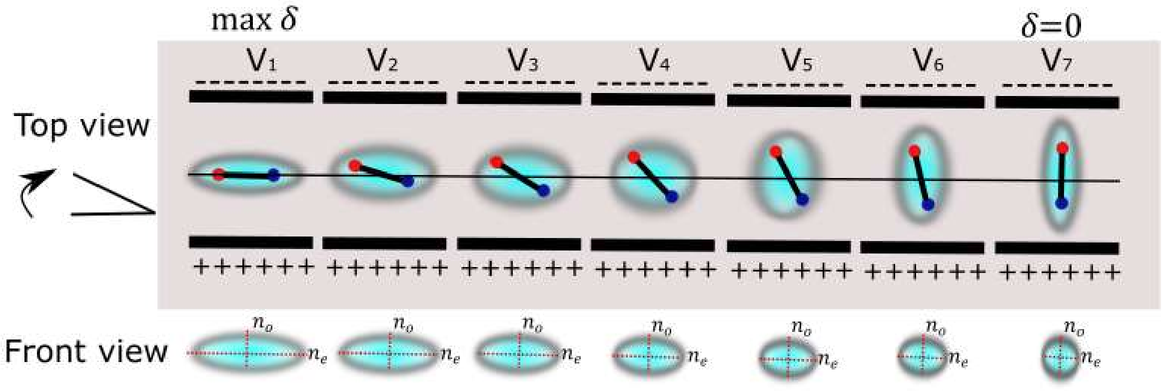

Fig. 3.1.3 Liquid crystal molecule reorienting, with an external electric field, top and front view.

This variable retardance permits a polarimeter to measure different polarization components without moving parts, and with a fast response time. A representation of the complete cell without any applied voltage is shown in Fig. 3.1.4, with an applied voltage is shown in Fig. 3.1.5.

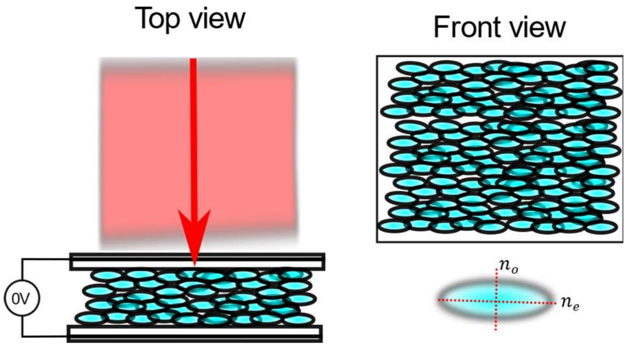

Fig. 3.1.4 Molecules inside a liquid crystal variable retarder, without any applied voltage.

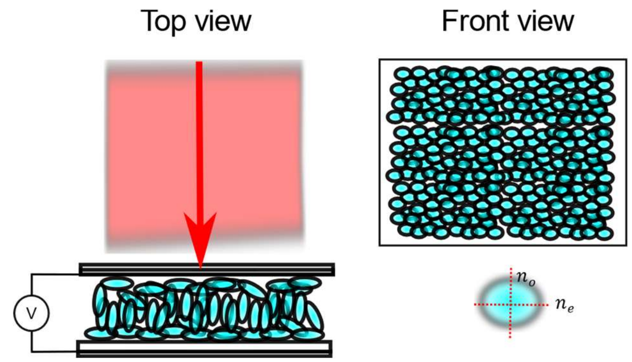

Fig. 3.1.5 Molecules inside a liquid crystal variable retarder, with an applied voltage.

The LCVRs used in this thesis are model LCC2415-VIS/M by Thorlabs. One of the LCVRs used is shown in Fig. 3.1.6

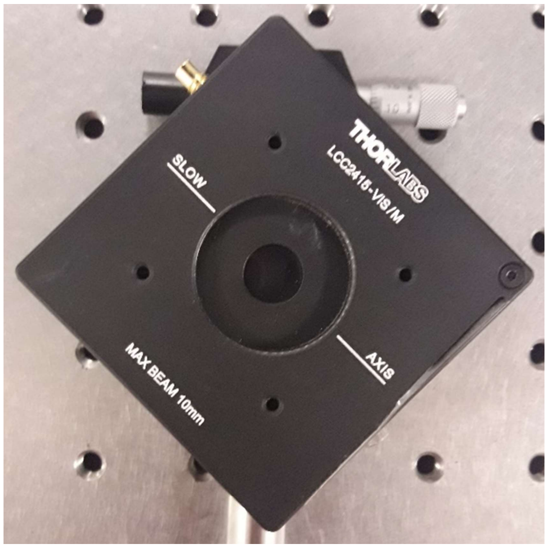

Fig. 3.1.6 Liquid crystal variable retarder by Thorlabs.

3.2 LCVR polarimetry

A design of a Stokes polarimeter based on two LCVRs is shown in Fig. 3.2.1. The light to be analyzed passes through the PSA, a pair of LCVRs and a polarizer, before entering the detector.

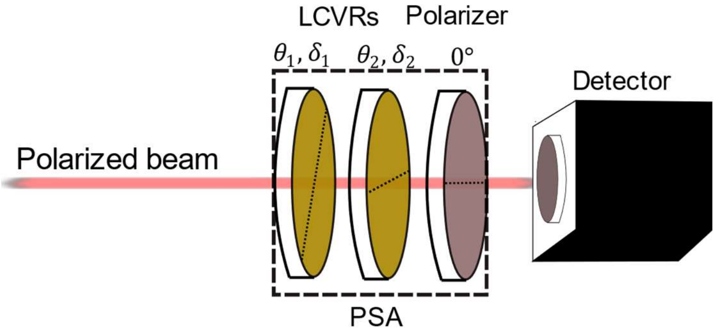

Fig. 3.2.1 Stokes polarimeter based on two LCVRs.

As mentioned in section 2.1, the Mueller matrix of an optical system, in this case the two LCVRs and the polarizer, can be described by the right to left product of the Mueller matrices individually,

$$\bar{\boldsymbol{M}}_{PSA(N)}(\theta_1, \delta_1, \theta_2, \delta_2) = \bar{\boldsymbol{M}}_{P}(0°)\bar{\boldsymbol{M}}_{R2}\left(\theta_2, \delta_2^{\mathrm{N}}\right)\bar{\boldsymbol{M}}_{R1}(\theta_1, \delta_1^{\mathrm{N}}), \tag{3.2.1}$$

where $\bar{\boldsymbol{M}}_{Rj}\left(\theta_j, \delta_j\right)$ is the Mueller matrix of the j-th LCVR, $\bar{\boldsymbol{M}}_{P}(0°)$ is the Mueller matrix of a horizontal linear polarizer, and $\bar{\boldsymbol{M}}_{PSA(N)}$ is the Mueller matrix of the polarimeter in the N-th configuration of the polarimeter. Then for this polarimeter the instrument matrix is defined as

$$\bar{\boldsymbol{A}} = \begin{pmatrix} \left[\bar{\boldsymbol{M}}_{pol}(0°)\bar{\boldsymbol{M}}_{R2}(\theta_2, \delta_2^1)\bar{\boldsymbol{M}}_{R1}(\theta_1, \delta_1^1)\right]_1 \\ \left[\bar{\boldsymbol{M}}_{pol}(0°)\bar{\boldsymbol{M}}_{R2}(\theta_2, \delta_2^2)\bar{\boldsymbol{M}}_{R1}(\theta_1, \delta_1^2)\right]_1 \\ \vdots \\ \left[\bar{\boldsymbol{M}}_{pol}(0°)\bar{\boldsymbol{M}}_{R2}\left(\theta_2, \delta_2^{\mathrm{N}}\right)\bar{\boldsymbol{M}}_{R1}(\theta_1, \delta_1^{\mathrm{N}})\right]_1 \end{pmatrix}, \tag{3.2.2}$$

where the subscript 1 in the brackets means the first row of the Mueller matrix of the polarimeter in the N-th configuration, which is related to the detected irradiance. The detected irradiance is dependent on the linear horizontal component of the light emerging from the second LCVR (S_1''), because of the polarizer placed just before the detector. Using the Mueller matrices for a retarder, shown in equation (2.1.20), the detected irradiance is directly related to

$$S_1'' = [\cos^2(2\theta_2) + \cos(\delta_2)\sin^2(2\theta_2)]S_1' +$$

$$\left[\left(1 - \cos(\delta_2)\right)\sin(2\theta_2)\cos(2\theta_2)\right]S_2' - [\sin(\delta_2)\sin(2\theta_2)]S_3', \tag{3.2.3}$$

where S_i' are the Stokes parameters emerging from the first LCVR. These parameters are related to the Stokes vector entering the polarimeter as

$$S_1' = [\cos^2(2\theta_1) + \cos(\delta_1)\sin^2(2\theta_1)]S_1^{inc} + \big[\big(1 - \cos(\delta_1)\big)\sin(2\theta_1)\cos(2\theta_1)\big]S_2^{inc} - [\sin(\delta_1)\sin(2\theta_1)]S_3^{inc}, \tag{3.2.4}$$

$$S_2' = \big[\big(1 - \cos(\delta_1)\big)\sin(2\theta_1)\cos(2\theta_1)\big]S_1^{inc} + [\sin^2(2\theta_1) + \cos(\delta_1)\cos^2(2\theta_1)]S_2^{inc} + [\sin(\delta_1)\cos(2\theta_1)]S_3^{inc}, \tag{3.2.5}$$

$$S_3' = [\sin(\delta_1)\sin(2\theta_1)]S_1^{inc} - [\sin(\delta_1)\cos(2\theta_1)]S_2^{inc} + [\cos(\delta_1)]S_3^{inc}. \tag{3.2.6}$$

The total irradiance in each measurement can be expressed as,

$$\begin{aligned} I_N = S_0^{inc} &+ \\ &S_1^{inc}\left[\big(\cos^2(2\theta_1) + A\sin^2(2\theta_1)\big)\big(\cos^2(2\theta_2) + C\sin^2(2\theta_2)\big)\right. \\ &\quad \left. + \Big(1/4\big((1-A)\sin(4\theta_1)\big)\big((1-C)\sin(4\theta_2)\big)\Big) - \big(DA\sin(2\theta_2)\sin(2\theta_1)\big)\right] + \\ &S_2^{inc}/2\left[\big(\cos^2(2\theta_2) + C\sin^2(2\theta_2)\big)\big((1-A)\sin(4\theta_1)\big)\right. \\ &\quad \left. +\big((1-C)\sin(4\theta_2)\big)\big(\sin^2(2\theta_1) + A\cos^2(2\theta_1)\big) + 2DB\sin(2\theta_2)\cos(2\theta_1)\right] + \\ &S_3^{inc}\left[\big(\cos^2(2\theta_2) + C\sin^2(2\theta_2)\big)\big(-B\sin(2\theta_1)\big)\right. \\ &\quad \left. +\big(1/2(1-C)B\sin(4\theta_2)\big)\big(\cos(2\theta_1)\big) - \big(DA\sin(2\theta_2)\big)\right], \end{aligned} \tag{3.2.7}$$

where $A = \cos(\delta_1^N), B = \sin(\delta_1^N), C = \cos(\delta_2^N), D = \sin(\delta_2^N)$. With this equation we can relate each measurement to a polarization state analyzed, depending on the experimental parameters of the LCVRs. Using equation (2.2.6), the instrument matrix in equation (3.2.2), and at least four measurements we can estimate the Stokes vector of any incident beam.

However, due to its liquid nature, the molecules in the LCVRs, have only a *preferential* orientation, which is not completely defined, so the director orientation can vary over the aperture. Also, the orientation changes with the applied voltage, this behavior has also been reported by other authors [29,30]. When an electric field is applied, we have to consider that this field is not completely uniform, nor are the changes in the molecules, as represented in Fig. 3.1.5, then the induced retardance will vary over the full aperture. These spatial variations have also been reported before [31,32]. Thus, the polarization measurements will differ from the ideal. Considering the variations mentioned before, on this thesis we will focus on the errors in the axis position and induced retardance in the LCVRs. In the next chapter we verify the performance of a Stokes polarimeter and estimate the Root Mean Squared Error (RMSE) values obtained with optimized and non-optimized schemes. Also, a calibration method is proposed and verified to compensate the mentioned errors.

4 Stokes polarimeter

To verify the performance of a Stokes polarimeter based on two LCVRS, we designed and implemented a polarimeter without an imaging system, based on the diagram shown in Fig. 3.2.1. The experimental set-up is shown in Fig. 4.0.1. This is a simpler set-up as a first approximation to the final objective, this system only uses a small part of the aperture of the LCVRs, unlike in an imaging system where the full aperture is used and the spatial variations are expected to be larger. We measured the Stokes parameters of three different samples and compared the obtained results using an optimized and a non-optimized polarimeter. The results were compared, showing smaller RMSE values when using an optimized polarimeter. Finally, to reduce the RMSE in the obtained results a calibration method is proposed. The method compensates variations in retardance and fast axis position of the LCVRs, with a fitting procedure.

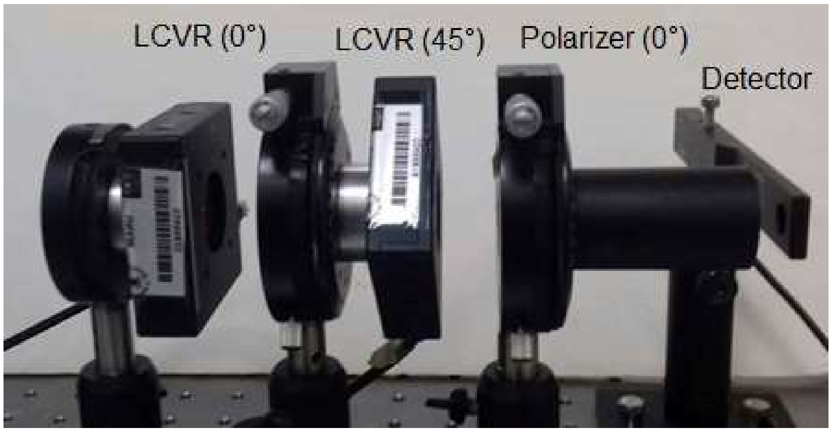

Fig. 4.0.1 Experimental set-up of the Stokes polarimeter.

4.1 Experimental results

The experimental set-up shown in Fig. 4.0.1 was tested in our laboratory. The first LCVR was mounted with its fast axis at 0°, and the second LCVR, with its fast axis at 45°. Then we can rewrite equation (3.2.7) as

$$I_N = \frac{1}{2}\left(S_0^{inc} + \cos\delta_2^N S_1^{inc} + \sin\delta_1^N \sin\delta_2^N S_2^{inc} - \cos\delta_1^N \sin\delta_2^N S_3^{inc}\right). \qquad (4.1.1)$$

The application of at least four combinations of retardance values to the LCVRs and equation (2.2.6) are used to extract all the Stokes parameters from irradiance data. This can be achieved by four combinations, that measure the irradiance of the linear horizontal, vertical, at +45°, and right circular, polarization components. These combinations are represented by the instrument matrix:

$$\bar{\boldsymbol{A}}_{4-\mathrm{m}} = \begin{pmatrix} \bar{\mathbf{M}}_{\mathrm{pol}}(0°)\bar{\mathbf{M}}_{\mathrm{R2}}(45°,360°)\bar{\mathbf{M}}_{\mathrm{R1}}(0°,90°) \\ \bar{\mathbf{M}}_{\mathrm{pol}}(0°)\bar{\mathbf{M}}_{\mathrm{R2}}(45°,180°)\bar{\mathbf{M}}_{\mathrm{R1}}(0°,90°) \\ \bar{\mathbf{M}}_{\mathrm{pol}}(0°)\bar{\mathbf{M}}_{\mathrm{R2}}(45°,90°)\bar{\mathbf{M}}_{\mathrm{R1}}(0°,90°) \\ \bar{\mathbf{M}}_{\mathrm{pol}}(0°)\bar{\mathbf{M}}_{\mathrm{R2}}(45°,90°)\bar{\mathbf{M}}_{\mathrm{R1}}(0°,360°) \end{pmatrix} = 1/2 \begin{pmatrix} 1 & 1 & 0 & 0 \\ 1 & -1 & 0 & 0 \\ 1 & 0 & 1 & 0 \\ 1 & 0 & 0 & 1 \end{pmatrix}. \qquad (4.1.2)$$

For this case the CN is 3.23 and the EWV is 16.00, but as mentioned in section 2.2.2 to reduce the effect of noise in the measurements on the final solution, the CN must be minimized to an optimal value of $\sqrt{3}$, or the EWV to an optimal value of $40/N$, in this case $N = 4$. The optimization of the polarimeter can be achieved with the same experimental set-up with two more measurements, giving a total of six measurements. The instrument matrix in this case is,

$$\bar{\boldsymbol{A}}_{6-\mathrm{m}} = \begin{pmatrix} \bar{\mathbf{M}}_{\mathrm{pol}}(0°)\bar{\mathbf{M}}_{\mathrm{R2}}(45°,360°)\bar{\mathbf{M}}_{\mathrm{R1}}(0°,90°) \\ \bar{\mathbf{M}}_{\mathrm{pol}}(0°)\bar{\mathbf{M}}_{\mathrm{R2}}(45°,180°)\bar{\mathbf{M}}_{\mathrm{R1}}(0°,90°) \\ \bar{\mathbf{M}}_{\mathrm{pol}}(0°)\bar{\mathbf{M}}_{\mathrm{R2}}(45°,90°)\bar{\mathbf{M}}_{\mathrm{R1}}(0°,90°) \\ \bar{\mathbf{M}}_{\mathrm{pol}}(0°)\bar{\mathbf{M}}_{\mathrm{R2}}(45°,90°)\bar{\mathbf{M}}_{\mathrm{R1}}(0°,270°) \\ \bar{\mathbf{M}}_{\mathrm{pol}}(0°)\bar{\mathbf{M}}_{\mathrm{R2}}(45°,90°)\bar{\mathbf{M}}_{\mathrm{R1}}(0°,360°) \\ \bar{\mathbf{M}}_{\mathrm{pol}}(0°)\bar{\mathbf{M}}_{\mathrm{R2}}(45°,90°)\bar{\mathbf{M}}_{\mathrm{R1}}(0°,180°) \end{pmatrix} = 1/2 \begin{pmatrix} 1 & 1 & 0 & 0 \\ 1 & -1 & 0 & 0 \\ 1 & 0 & 1 & 0 \\ 1 & 0 & -1 & 0 \\ 1 & 0 & 0 & 1 \\ 1 & 0 & 0 & -1 \end{pmatrix}, \qquad (4.1.3)$$

where the CN is 1.73 and the EWV is 6.67, in this case we have an optimized polarimeter, with $N = 6$. With a non-optimized polarimeter, the CN and EWV have an increment of 87% and 139% from the optimal values obtained with six measurements. To test the polarimeters we measure the Stokes parameters of a light beam emerging from three different rotating samples: a linear polarizer, a half-wave plate and a quarter-wave plate. As light source we used a 633 nm He-Ne laser, with a collimated beam spot of $(0.837 \pm 0.003)\ mm$ in diameter. The light passed through a beam splitter to yield an auxiliary beam to monitor and eliminate variations due to the laser instability. Then the light passed through a linear polarizer to ensure that the incident light on the sample was polarized. After the sample, the light beam entered the Stokes polarimeter. The detector used in this thesis is model S120C, by Thorlabs. We measured the irradiance for the six configurations of the optimized polarimeter, rotating the axes of the samples from 0° to 180° in 10° increments. In Fig. 4.1.1 we show the typical irradiance measurements for a given sample, in this case the half-wave plate measurements are presented.

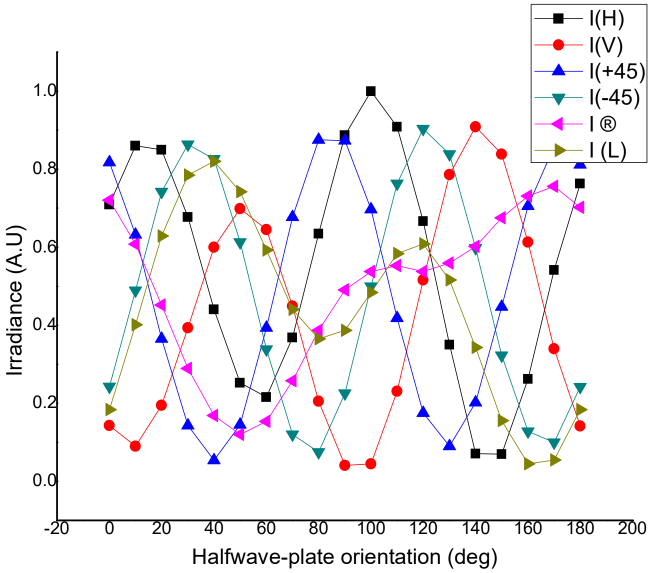

Fig. 4.1.1 Irradiance measurements for the half-wave plate.

Using four irradiance measurements, equation (2.2.6) and the instrument matrix shown in equation (4.1.2), we can estimate the Stokes parameters for every axis orientation for each sample. We also estimate the Stokes parameters using the six measurements and equations (2.2.7) and (4.1.3), which leads to an optimized polarimeter. Then we calculated the RMSE, between the theoretical and the experimentally estimated Stokes parameters for both cases. The RMSE is defined as

$$\mathrm{RMSE} = \sqrt{\frac{1}{M_\theta}\sum_{m=1}^{M_\theta}\left(S_i^{exp} - S_i^{theo}\right)_m^2}, \tag{4.1.4}$$

where the superscript *exp* denotes the experimental values, the superscript *theo* denotes the theoretical (ideal or expected) values. The subscript i indicates a particular Stokes parameter, the subscript m indicates the angle at which the Stokes vector is calculated and there are M_θ rotation angles in the measurement of each Stokes vector. The results obtained from this experiment are shown in Fig. 4.1.2

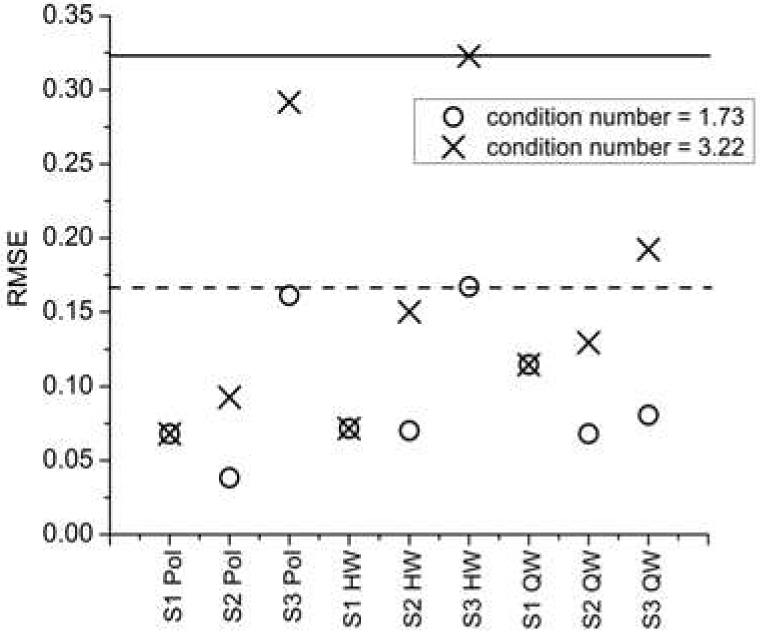

Fig. 4.1.2. RMSE in the measured Stokes parameters with an optimized (circles), and non-optimized (crosses) polarimeter. The x-axis indicates the element of the Stokes vector and the sample used: Pol is the linear polarizer, HW is the half-wave plate, and QW is the quarter-wave plate.

From Fig. 4.1.2 it can be seen that there is a larger RMSE in the non-optimized polarimeter. In both polarimeters the parameter S_3 has the largest RMSE values for each sample. The first two rows, or measurements, of the two instrument matrices are the same, which are related to the parameter S_1, so the RMSE for this parameter is the same. The solid horizontal line marks the maximum RMSE (0.323) for a non-optimized polarimeter and the dashed line the maximum (0.167) for an optimized polarimeter. In table 4.1.1 we show the average and standard deviation of the RMSE values in both polarimeters.

	$Optimized\ polarimeter$ $k = 1.73{:} EWV = 6.67$	$Non - optimized\ polarimeter$ $k = 3.22{:} EWV = 16.00$
Average RMSE	0.09 ± 0.04	0.16 ± 0.09

Table 4.1.1 RMSE in an optimized and a non-optimized polarimeter.

From table 4.1.1 we can see that the average RMSE increases by 70% with the non-optimized polarimeter, which is a significant reduction in the accuracy. Also, the standard deviation increases by 106%, which means that the accuracy varies for different Stokes parameters. So, an increment in the optimization metric of the instrument matrix leads to larger RMSE values. Although the analysis was performed for only two condition numbers, the results are clear and show that the minimization of the optimization metric is essential in polarimetric measurements.

However, even with the optimized polarimeter, the accuracy and precision of the polarimeter are not as expected. This could be due to the fact that the optimization only considers noise, but the instrumental errors are ignored. A calibration can help to reduce the RMSE in the measurements, considering the experimental errors. In the next section we present and verify a novel method that compensates errors in the polarimeter and calibration samples, to obtain more accurate and precise results.

4.2 Calibration method

A calibration method requires an analysis of the results obtained with a number of known polarization calibration samples. The detected irradiances or the measured Stokes parameters are then compared to the ideal cases to deduce the errors in the system and the corrections required to obtain accurate results. In this thesis we propose the use of either four or six calibration samples, and we compare the results of the two cases. As calibration samples, for the case of six samples we used a horizontal linear polarizer, a vertical linear polarizer, a half-wave retarder with its axes at 30° and at 60°, and a quarter-wave retarder with its fast axis at 30° and at 60°. These values of the angles of the axes of the fixed retarder plates were chosen to have contributions in as many as possible of the elements in the generated Stokes vectors. For the case of four calibration samples, we chose a horizontal linear polarizer, a vertical linear polarizer, a half-wave retarder with its fast axis at 30°, and a quarter-wave retarder with its fast axis at 30°. With these samples, in both cases we obtain contributions in the four Stokes parameters. Using an optimized polarimeter and six calibration samples we have 36 irradiance measurements. With a non-optimized polarimeter and four calibration samples we have only 16 irradiance measurements. Obviously, this second case has the advantage of fewer measurements, which means a shorter measurement time. However, as shown below, there is an adverse effect on the final measurement precision.

The calibration procedure proposed consists of two stages. In the first stage the experimental errors in the set-up are calculated by fitting the experimental irradiance measurements for the calibration samples to the theoretical polarimeter with errors. This is performed by using a non-linear fitting procedure with the experimental errors as the fitting parameters, and the sum of the differences between the experimental irradiances and the calculated model irradiances, including experimental errors, as the metric to be minimized. The measured irradiances were fitted to the theoretical model with the error parameters using a computer program developed in our laboratory, and the "Powell" algorithm [33]. Fitting algorithms need a starting solution, and we used an ideal experimental set-up, without errors, as the starting value. The errors introduced in the polarimeter model to replicate the measured irradiances were: errors in each of the orientation angles of the LCVR axes, and errors for each different value of the retardance of each LCVR. This means that, for the optimized polarimeter, equation (4.1.3), there are four different retardance values for LCVR 1, and three different values of retardance for LCVR 2, giving a total of seven retardance errors. For the non-optimized case, there are 2 retardance values for LCVR 1, and again 3 for LCVR 2, giving a total of five retardance errors for this case. We also included errors in the axes positions of the calibration samples, giving one error for each sample. This means that the case of an optimized polarimeter and six calibration samples has 15 error terms, and so 15 fitting parameters in our method. For a non-optimized polarimeter and only four calibration samples, we have a total of 11 fitting parameters. The metric, M, used in the fitting procedure is the rms difference between the experimental and expected (theoretical) irradiances over all the calibration samples and all of the polarimeter configurations:

$$M = \left(\sum_{i=1}^{N} \sum_{j=1}^{n} \frac{1}{Nn} \left(S_0^{exp} - S_0^{theo}\right)^2\right)^{1/2}, \tag{4.2.1}$$

where the superscript *exp* denotes the experimentally measured irradiance, the superscript *theo* denotes the theoretical irradiance from the model of the polarimeter with errors, *n* indicates the number of calibration samples used (in our case 4 or 6), *N* denotes the number of irradiances detected for the N configurations of the polarimeter, for each sample, and this metric is minimized in the fitting procedure. The second step of the proposed method takes the fitting parameters optimized in the first step and assumes that they represent the fixed systematic experimental errors. Then we use the irradiance measurements of the unknown sample beam to obtain its complete Stokes vector, by fitting using the difference between the calculated and measured intensities as metric, and the four Stokes parameters as the fitting parameters. In this case we have four unknowns, the Stokes parameters, and either six irradiances, for the optimized case, or four irradiances, for the non-optimized case. The metric, M', in this case is

$$M' = \left(\sum_{i=1}^{N} \sum_{j=1}^{4} \frac{1}{4N} \left(S_0^{exp} - S_0^{theo}\right)^2\right)^{1/2}. \tag{4.2.2}$$

To verify the calibration method, the results shown in the previous section were the initial values to be calibrated. The calibrated results with four calibration samples are shown in Fig. 4.2.1. The solid horizontal line marks the maximum RMSE (=0.561) for a non-optimized polarimeter and the dashed line the maximum (=0.086) for an optimized polarimeter. The results using six calibration samples are shown in Fig.

4.2.2. Also, the solid horizontal line marks the maximum RMSE (=0.223) for a non-optimized polarimeter and the dashed line the maximum (=0.077) for an optimized polarimeter.

Fig. 4.2.1 and 4.2.2 show the same results as Fig. 4.1.2 but calibrated with four and six calibration samples, respectively. After applying the calibration method, for an optimized polarimeter, the maximum RMSE is reduced by 48% and 51% using four and six calibration samples, respectively. For a non-optimized polarimeter and using six samples the maximum RMSE is reduced by 30% but using four calibration samples the maximum RMSE increases. In table 4.2.1 we show the average RMSE before and after calibrating the results, with six and four calibration samples.

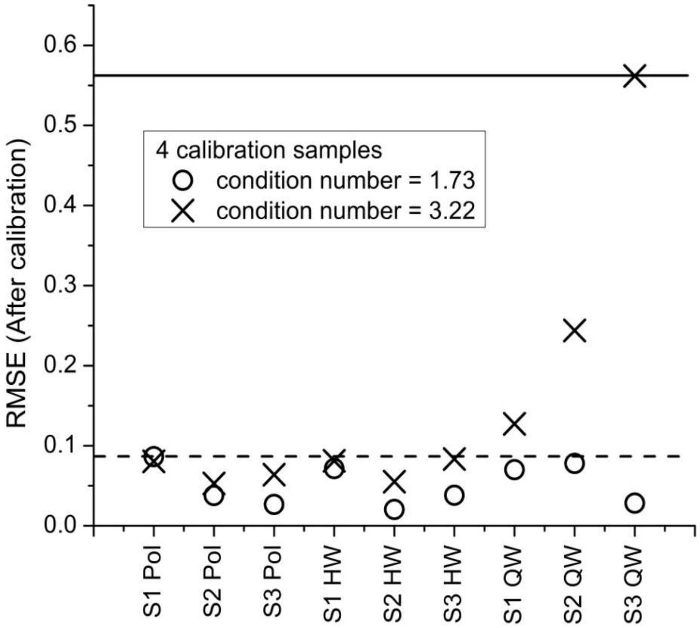

Fig. 4.2.1. RMSE in calibrated measured Stokes parameters with an optimized (circles), and non-optimized polarimeter (crosses), using four samples in the calibration process. The x-axis indicates the element of the Stokes vector and the calibration sample used: Pol is the linear polarizer, HW is the half-wave retarder plate, and QW is the quarter-wave retarder plate.

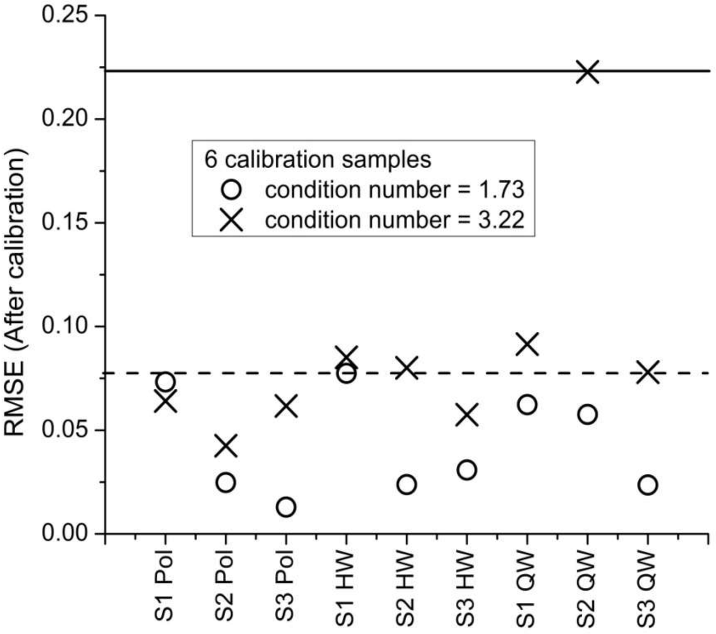

Fig. 4.2.2. RMSE in calibrated measured Stokes parameters with an optimized (circles), and non-optimized polarimeter (crosses), using six samples in the calibration process. The x-axis indicates the element of the Stokes vector and the calibration sample used: Pol is the linear polarizer, HW is the half-wave retarder plate, and QW is the quarter-wave retarder plate.

Average RMSE	$Optimized\ polarimeter$ $k = 1.73, EWV = 6.67$	$Non - optimized\ polarimeter$ $k = 3.23, EWV = 16.00$
Experimental	0.09 ± 0.04	0.16 ± 0.09
Calibrated with 4 samples	0.05 ± 0.02	0.15 ± 0.16
Calibrated with 6 samples	0.04 ± 0.02	0.09 ± 0.05

Table 4.2.1. Average RMSE and standard deviation in the calibrated results.

It can be seen that the calibration method proposed fails when it is used with a non-optimized polarimeter, and four calibration samples, leading to similar RMSE results but with a bigger standard deviation. When using a non-optimized polarimeter and six calibration samples the average RMSE is reduced by 44%, however these results are very similar to the results obtained with an optimized polarimeter without a calibration. The best results are obtained in the case of an optimized polarimeter, with a reduction in the average RMSE of 44% with four calibration samples and 55%

with six calibration samples. Even though the method works properly with the non-optimized polarimeter and six calibration samples, comparing with the optimized polarimeter shows that it is not recommended.

To verify the performance of the calibration method, with an optimized polarimeter we made 3 sets of 9 Stokes parameter measurements using an optimized polarimeter and six calibration samples. But before each measurement the LCVRs were recharacterized, the experimental set-up was reassembled, and the calibration samples were measured. The calibration calculation was applied each time we measured the complete Stokes vector of the three rotating samples. These test runs show the stability of the experimental setup and of the calibration method proposed. The results of these measurements are shown in Fig. 4.2.3.

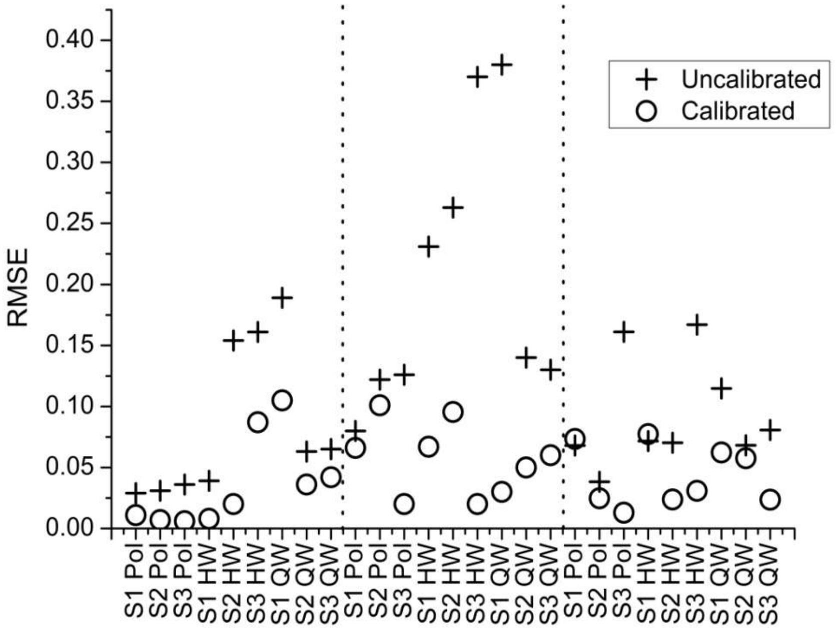

Fig. 4.2.3. RMSE of measured Stokes parameters, before (crosses) and after (circles) applying the calibration method, using six calibration samples, with an optimized polarimeter. The x-axis indicates the element of the Stokes vector and the calibration sample used: Pol is the linear polarizer, HW is the half-wave retarder plate, and QW is the quarter-wave retarder plate. The vertical dotted lines separate the different test runs performed.

We can see from Fig. 4.2.3, that the parameters S_1 and S_3 have the biggest RMSE values with the experimental results without a calibration. Also, that the precision of the final results changes with alterations in the experimental system. However, with the calibration process proposed here nearly all of the RMSEs after the calibration are less than those before the calibration. There are two values of RMSE in the third test run that have a larger RMSE after calibration, but the absolute value of the changes in RMSE is small (in the third decimal place) for both cases. The worst case RMSE after the calibration is 0.105, and the RMSE is reduced by the calibration between 17% and 94.5%. Figure 4.2.4 shows the percentage reduction in the RMSE with our calibration procedure as a function of the uncalibrated RMSE.

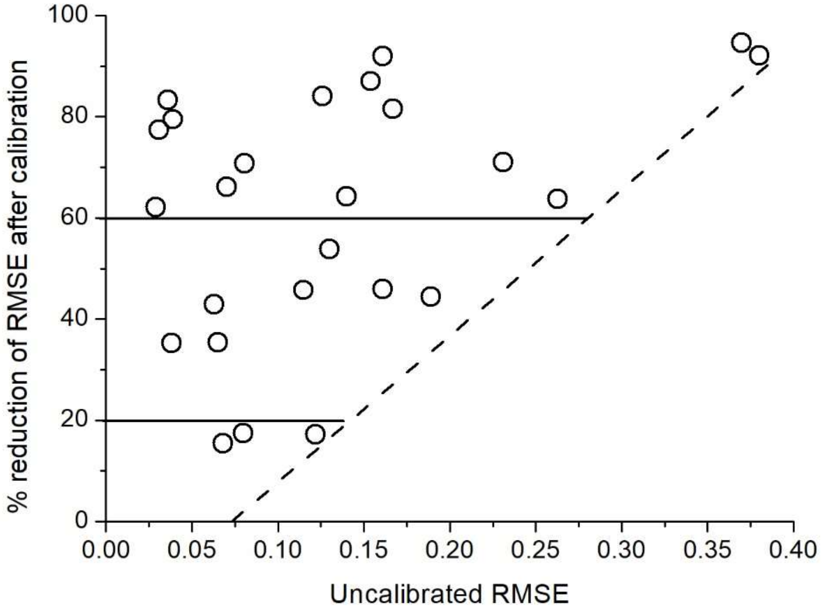

Fig. 4.2.4. The percentage reduction of the RMSE as a function of uncalibrated RMSE, showing that higher values of the uncalibrated RMSE tend to have a higher correction percentage. The dotted line is drawn as an aid for visualization of the tendency.

This figure shows that most of the measurements have reductions above 60% for any value of the uncalibrated RMSE. All values below 20% of reduction of the RMSE appear for uncalibrated RMSE values that are already lower than about 0.12. This figure also shows that higher values of the uncalibrated RMSE tend to have larger percentage reductions in the calibrated RMSE, as shown by the dashed line drawn on the graph as an aid to visualization. In table 4.2.2 we present the average RMSE before and after the calibration, showing a significant reduction in the average and in the standard deviation, which means an enhancement in the accuracy and precision of the polarimeter.

	$Before\ calibration$	$After\ calibration$
Average RMSE	0.13 ± 0.09	0.04 ± 0.03

Table 4.2.2. Average RMSE before and after the calibration.

The experimental data for an optimized polarimeter and six calibration samples, yield very good results, having a reduction of 69% in the average RMSE and of 66% in the standard deviation, after the calibration. The results for a non-optimized polarimeter are also improved using the proposed calibration method, although these improvements are not enough for the final measurements. These results show that this method can help compensate instrumental errors in the measurements of the Stokes vectors, but only for optimized schemes. The results presented in this chapter are clear and show that the optimization and calibration are essential in polarimetric measurements

5 Stokes imaging polarimeter

With the same basic structure as the PSA, shown in section 3.2, we designed a Stokes imaging polarimeter, the diagram of the set-up is shown in Fig. 5.0.1. To acquire the polarimetric images we used two lenses along with a CCD camera. The light emerging from the object is collimated with an achromatic lens, which gives parallel rays between the two lenses. In this parallel beam path, we can insert our PSA, and the second lens is focused on the CCD camera to record the image.

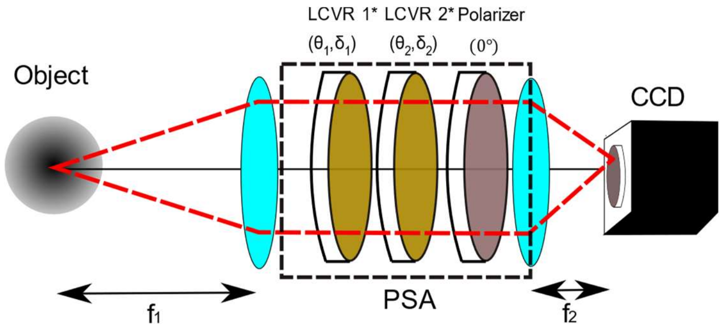

Fig. 5.0.1. Diagram of the set-up of a Stokes imaging polarimeter based on two LCVRs.

To reduce the measurement time, we decided to use only four measurements but with an optimized scheme, the retardance values and axes positions used in the polarimeter were obtained following the procedure presented by De Martino et. al. [34]. The configuration used can be expressed by the following instrument matrix,

$$\bar{\boldsymbol{A}}_1 = \begin{pmatrix} \bar{\boldsymbol{M}}_{pol}\bar{\boldsymbol{M}}_{R2}(27.4°, 315°)\bar{\boldsymbol{M}}_{R1}(72.4°, 135°) \\ \bar{\boldsymbol{M}}_{pol}\bar{\boldsymbol{M}}_{R2}(27.4°, 135°)\bar{\boldsymbol{M}}_{R1}(72.4°, 135°) \\ \bar{\boldsymbol{M}}_{pol}\bar{\boldsymbol{M}}_{R2}(27.4°, 135°)\bar{\boldsymbol{M}}_{R1}(72.4°, 315°) \\ \bar{\boldsymbol{M}}_{pol}\bar{\boldsymbol{M}}_{R2}(27.4°, 315°)\bar{\boldsymbol{M}}_{R1}(72.4°, 315°) \end{pmatrix} = \frac{1}{2}\begin{pmatrix} 1 & 0.47 & -0.33 & -0.82 \\ 1 & -0.94 & -0.33 & 0.00 \\ 1 & 0.00 & 1.00 & 0.00 \\ 1 & 0.47 & -0.33 & 0.82 \end{pmatrix}. \quad (5.0.1)$$

With this configuration the CN of this matrix is 1.732, and the EWV is 10, which are very close to the optimized values, with four measurements. In this experimental set-up it is important to consider that the full aperture of the LCVRs is used, unlike the set-up presented in chapter 4. As mentioned before we do not expect a uniform retardance in the complete aperture, due to the structure of the liquid crystal cell;

also in previous characterizations we have detected differences while characterizing LCVRs between methods using an unexpanded, and an expanded laser beam. These effects can be attributed to spatial variations over the clear aperture of the LCVRs, leading to a different instrument matrix in different points of the aperture. In section 5.1 we propose a method to characterize the induced retardance over the complete aperture of each LCVR. In section 5.2, using the results of the characterization and the proposed scheme, we implemented and tested the performance of the Stokes imaging polarimeter shown in Fig. 5.0.2.

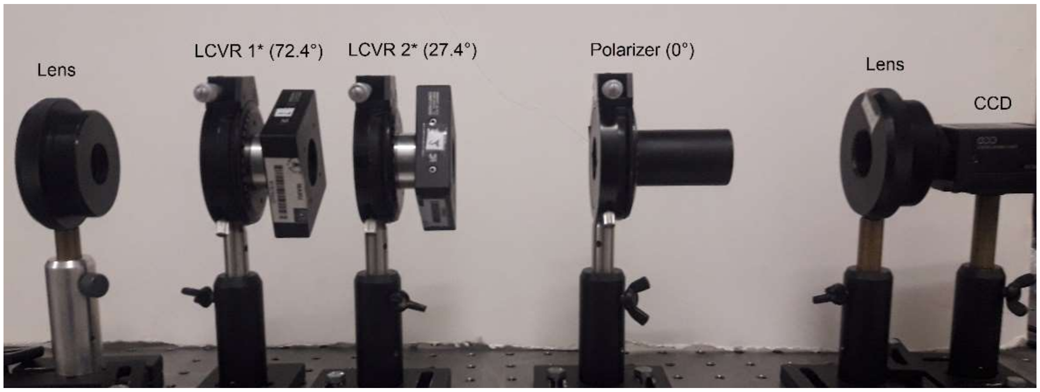

Fig. 5.0.2. Experimental set-up of the Stokes imaging polarimeter based on two LCVRs.

5.1 LCVR Characterization

A correct and complete characterization of the induced retardance over the full aperture of the LCVRs is very important. Previously, we had characterized the retardance using a photodetector to measure the irradiance of the direct beam from a laser, illuminating only a small part of the clear aperture. We also used a spatial filter to expand and clean the laser beam, to illuminate the complete aperture of the LCVRs and calculate the retardance by focusing all the light on the same photodetector. We found differences between the characterization for these two configurations, and as we mentioned before this suggests that there are variations of the retardance over the aperture of the LCVRs. Here we propose a method to measure the retardance as a function of the applied voltage using a CCD camera and a lens to obtain the retardance pixel by pixel over the complete aperture of a

LCVR. With this characterization we have higher accuracy and control of the retardances obtained for each applied voltage, and the magnitude of the spatial phase variations in the LC.

Before the retardance characterization, it is necessary to find the optical axes position of each LCVR, which are related to the director of the molecules. We performed a simple experiment, using two linear polarizers with their transmission axis crossed, and the LCVR placed between both polarizers. Then the LCVR is rotated until a minimum irradiance is reached, in this position the slow or fast axis is parallel to the transmission axis of the first polarizer. Considering the direction of the slow axis marked by the manufacturer, we can differentiate the slow from the fast axis. We applied voltages in a range from 1.5 to 8 volts in steps of 0.25 volts and measure the slow-axis position in each applied voltage. The relative axis position was plotted versus the applied voltage, the graphs for each LCVR are shown in Fig. 5.1.1 and 5.1.2.

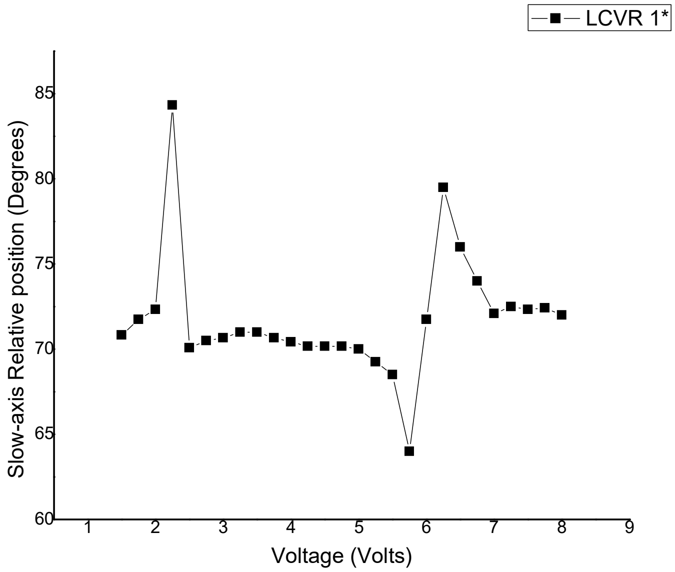

Fig. 5.1.1. Slow-axis relative position as a function of the applied voltage, for LCVR 1*.

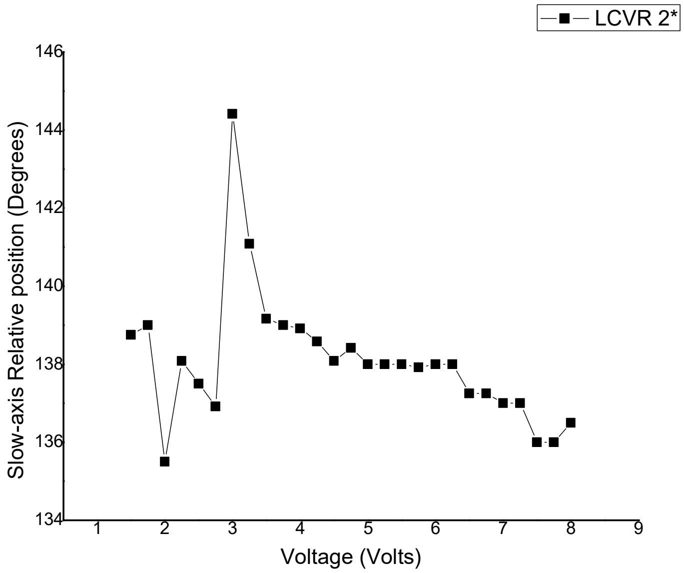

Fig. 5.1.2 Slow-axis relative position as a function of the applied voltage, for LCVR 2*.

For LCVR 1*, we found that the average axis position varies with a standard deviation of 3.62°, and for the LCVR 2*, the standard deviation is 1.72°. These results consider variations in the axis position due to the applied voltage, there are also spatial variations that have to be considered due to variations in the director of each molecule. To obtain the retardance as a function of the applied voltage, over the full aperture of the LCVRs, we used the set-up shown in Fig. 5.1.3.

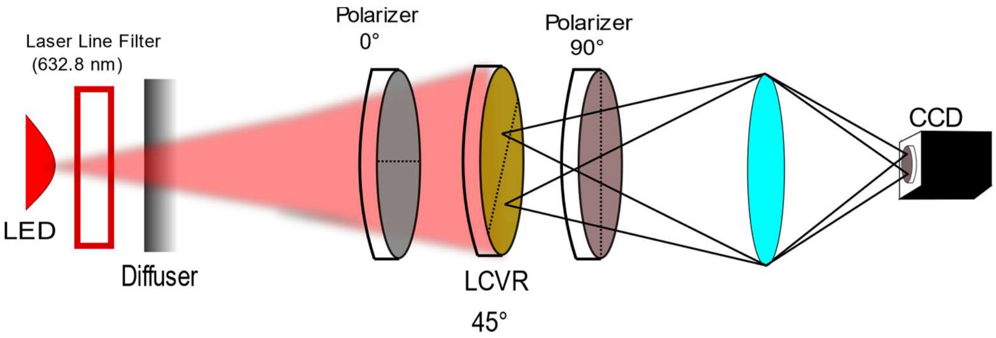

Fig. 5.1.3. Experimental set-up to characterize the induced retardance in a LCVR.

We use a LED as a light source, the light passes through a laser line filter (632.8 nm) and a diffuser to illuminate the LCVR with uniform intensity. The LCVR is placed with its fast axis at 45° from the horizontal plane, between two crossed linear polarizers, with their optical axes at 0° and 90°, respectively. A lens is placed after the second polarizer to focus the LCVR image on the CCD camera and the irradiance is measured for every pixel. In terms of Mueller matrices this optical system can be represented as

$$M_s = M_P(90°)M_R(\delta, 45°)M_P(0°), \tag{5.1.1}$$

where M_s is the Mueller matrix of the system, $M_P(\theta)$ is the Mueller matrix of a linear polarizer with its transmission axis at an angle of θ, and $M_R(\delta, \theta)$ is the Mueller matrix of a retarder with retardance δ and fast axis at θ. The Mueller matrix of this system is,

$$\boldsymbol{M}_S = 1/4\begin{pmatrix} 1-\cos(\delta) & 1-\cos(\delta) & 0 & 0 \\ -1+\cos(\delta) & -1+\cos(\delta) & 0 & 0 \\ 0 & 0 & 0 & 0 \\ 0 & 0 & 0 & 0 \end{pmatrix}. \tag{5.1.2}$$

Considering the light emerging from the LED is unpolarized, the incident Stokes vector, $\boldsymbol{S}_i$, is

$$\boldsymbol{S}_i = \begin{pmatrix} 1 \\ 0 \\ 0 \\ 0 \end{pmatrix}. \tag{5.1.3}$$

Using these equations, the emerging Stokes vector is

$$\boldsymbol{S} = A\begin{pmatrix} 1-\cos\delta \\ -1+\cos\delta \\ 0 \\ 0 \end{pmatrix}, \tag{5.1.4}$$

where A is a constant that depends on the factor ¼ of the matrix M_S, and also on the experimental parameters such as absorption of the polarizers. Considering that the irradiance is related to the first Stokes parameter we find that the detected irradiance on the CCD is

$$I = A(1-\cos\delta). \tag{5.1.5}$$

Additionally, we know that the maximum irradiance is obtained when $\cos\delta = -1$, then $I_{max} = 2A$, therefore

$$\delta = \cos^{-1}\left(1-\frac{2I}{I_{max}}\right). \tag{5.1.6}$$

With this equation the retardance value can be obtained, using the experimental data of the relative irradiance of the detected light as a function of the applied voltage. We applied different values of voltages to each LCVR based on previous results and on the retardance values required in equation (5.0.1). The range of applied voltages used in each LCVR is shown in table 5.1.1, the measurements were made in steps of 0.05 V.

LCVR	Voltage range (V)
LCVR 1*	2.15–- 3.8
LCVR 2*	2.9 – 5

Table 5.1.1. Intervals of applied voltages used to characterize each LCVR.

An example of the retardance maps obtained with this method, for different voltages in LCVR 1*, are shown in Fig. 5.1.4.

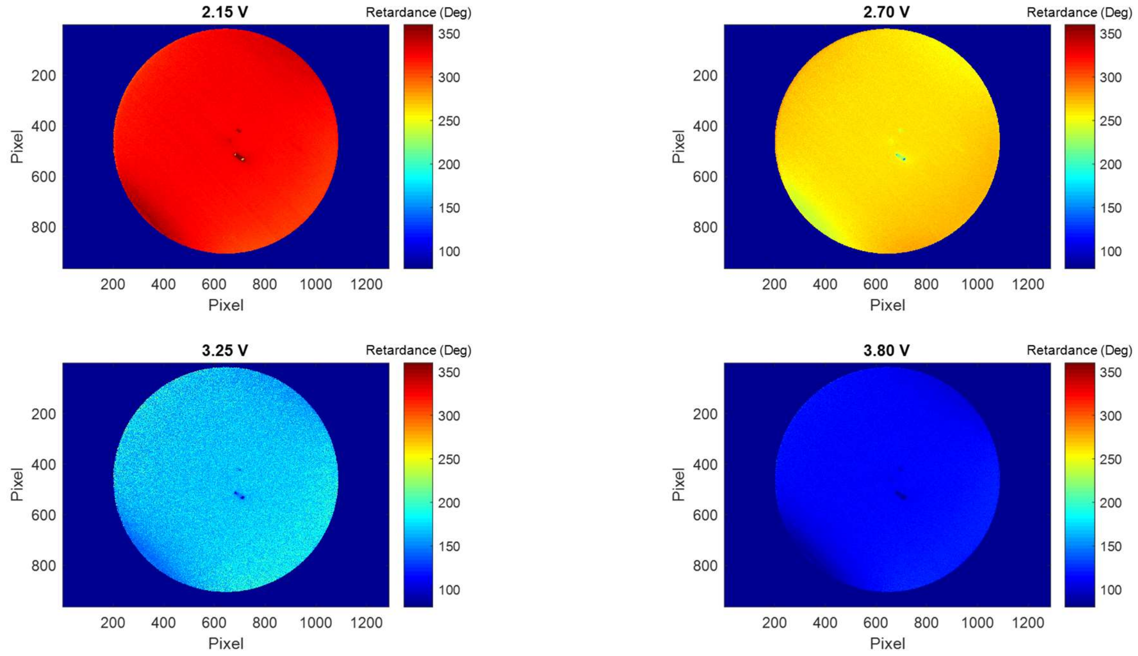

Fig. 5.1.4. Example of retardance maps obtained for a LCVR with different applied voltages.

We calculated the mean value and standard deviation over the full aperture for every applied voltage. In Fig. 5.1.5, we present the mean value as a function of the applied voltage for each LCVR. In Fig. 5.1.6, the standard deviation as a function of the retardance value is shown.

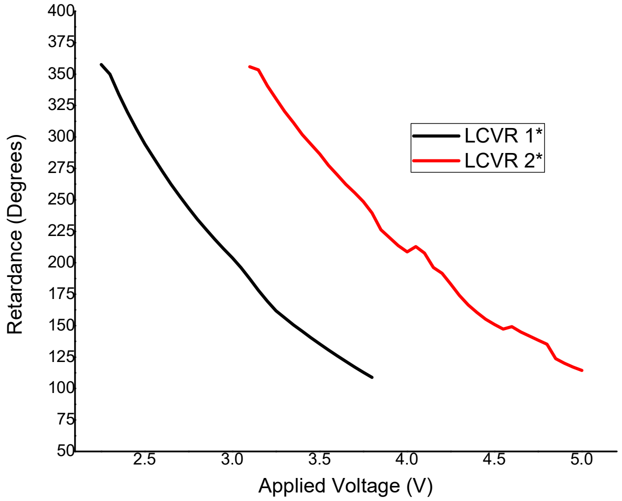

Fig. 5.1.5. Mean values of the retardance as a function of the applied voltage in the LCVR 1*(Black) and LCVR 2*(Red).

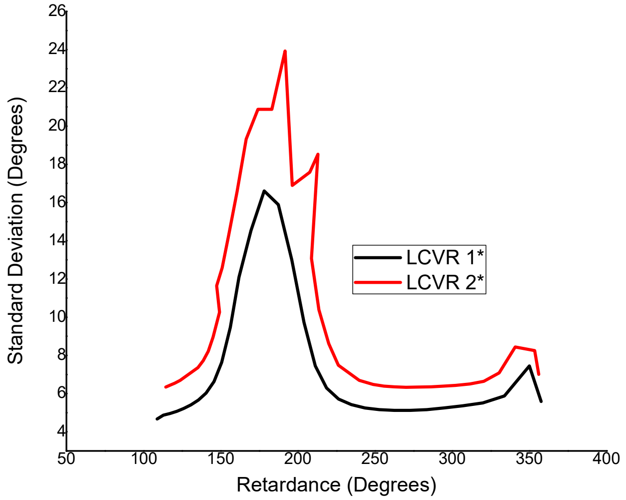

Fig. 5.1.6. Standard deviation as a function of the induced retardance in the LCVR 1*(Black) and LCVR 2*(Red).

From Fig. 5.1.5 we can see that the behavior is similar in both cases, with a displacement, but the behavior seems more unstable for LCVR 2* than for LCVR 1*, for which the graph is smoother. These results show that is necessary to perform an individual characterization of every used LCVR. Fig. 5.1.6 shows an average standard deviation over the measured interval of 7.3° and 10.3°, however in both cases we have a large peak around the retardance value of 180°, where the standard deviation reaches a value of 16.6° for LCVR 1* and 23.9° for LCVR 2*. If we consider the error propagation of equation (5.1.6) we obtain,

$$(\sigma_\delta)^2 = (\sigma_I)^2\left(\frac{1}{I_{max}\sqrt{\frac{I_{max}(I-I_{max})}{I^2}}}\right)^2 + (\sigma_{Imax})^2\left(\frac{1}{I_{max}^2\sqrt{\frac{I(I_{max}-I)}{I_{max}^2}}}\right)^2. \qquad (5.1.7)$$

In Fig. 5.1.7 we plotted the behavior of equation (5.1.7) varying the relative measured irradiance (left) and the maximum irradiance (right). From these graphs we can see that the error in the retardance has a maximum value when the measured irradiance is near 0 or near the maximum value. This means that the error will be maximum when the induced retardance has values of 0°, 180°, or 360°, which explains the peaks of the graph shown in Fig. 5.1.6. It can also be seen from the figure on the right that a bigger maximum irradiance can help to reduce the error propagation.

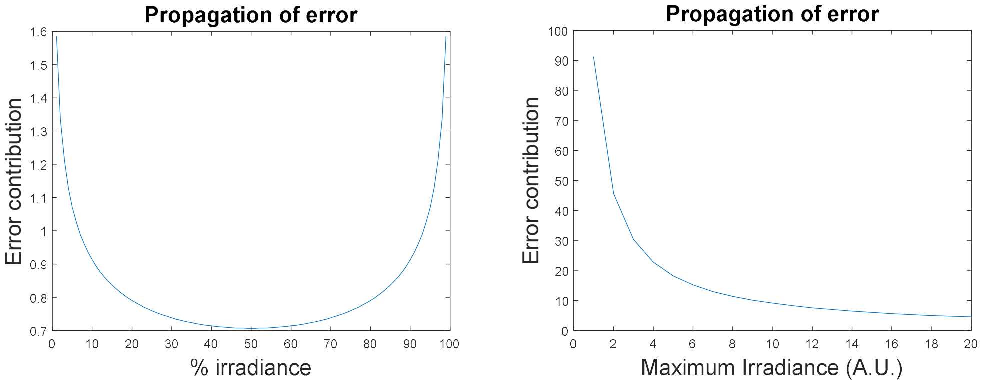

Fig. 5.1.7. Error propagation with a varying measured irradiance and maximum irradiance.

This analysis suggests that the variations of the larger peak in Fig. 5.1.6 is more related to the measurement process than to the LC properties. If we do not consider values around 180°, in a range from 165° to 195°, the average standard deviation in the rest of the interval is 6.2° for LCVR 1* and 8.8° for LCVR 2*, these results approximately agree with the manufacturer's specification, where they mention a variation of less than 7.2° [35].

Considering the results presented in this section and a slightly larger error due to effects that we were not able to measure, such as spatial variations in the axis position or due to temperature changes, in table 5.1.2 we show the errors that we will consider in the use of LCVRs.

Axis position	Induced retardance
$\theta \pm 4°$	$\delta \pm 9°$

Table 5.1.2. Errors considered in LCVRs.

In particular, in the next section, we develop an optimized Stokes imaging polarimeter based on the experimental set-up shown in Fig. 5.0.1, using only four measurements. The configuration represented by equation (5.0.1), used for the imaging polarimeter, uses only two retardance values in each LCVR: 135° and 315°. The detailed retardance maps for these induced retardances are shown in Fig. 5.1.8 for each LCVR.

In Fig. 5.1.8, it is clear that there is a small defect in the center region of LCVR 1*. It can be also seen that there are larger variations in the zones near the edges of the clear aperture. With a smaller voltage, where the retardance is larger, we can see diagonal "line" structures that are possibly due to organization of the directors of the long molecule direction parallel to the figure, while with a larger voltage this structure is less visible since in this case the molecules are tilted, and the director of the molecules is shorter in the plane of the figure.

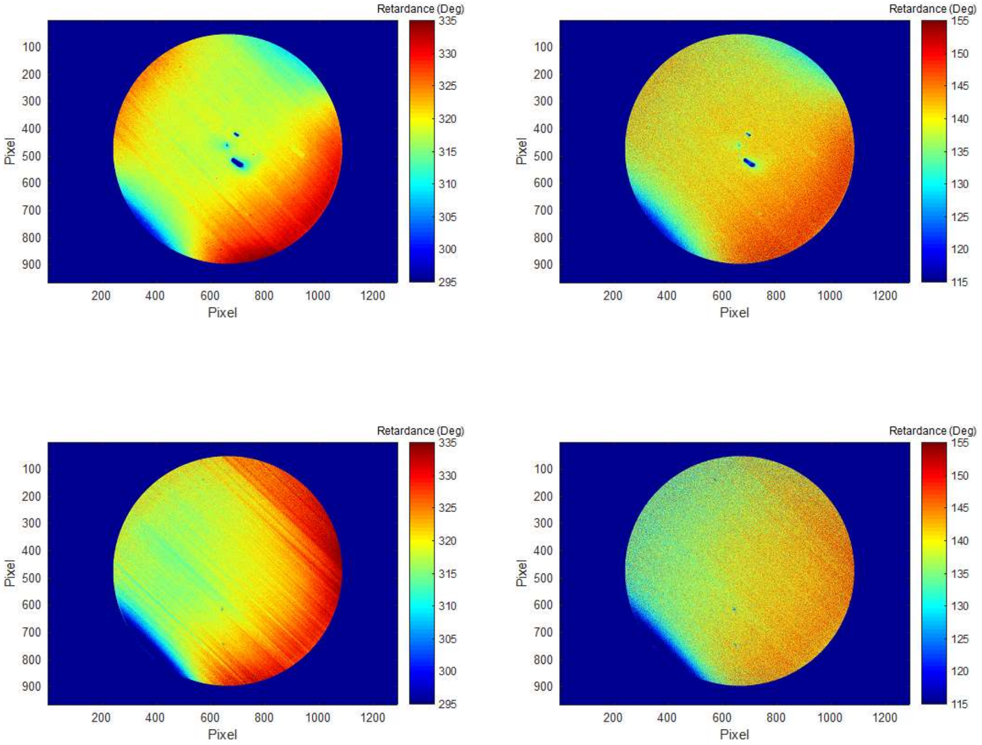

Fig. 5.1.8. Retardance maps for the two applied voltages, 315° (Left) and 135° (Right) of the complete aperture, of LCVR 1*(Top), and LCVR 2* (Bottom)

In this section an experimental method to characterize the retardance over the full aperture of LCVRs as a function of the applied voltage was proposed. With this characterization we were able to measure the errors in the axis position and in the induced retardance of the LCVRs, mentioned at the end of section 3.2. We also have a better control of the voltages needed to obtain the induced retardances used in the optimized polarimeter scheme, presented in the next section

5.2 Polarimetric images

To test our experimental set-up and characterization, we implemented the experimental set-up shown in Fig. 5.0.2, represented by the instrument matrix in equation (5.0.1). We used a set of four optimized calibration polarization samples obtained using a polarizer along with a quarter-wave plate [36]. We used a LED along with a diffuser and a laser line filter as light source, then the light reaches the polarizer and finally the quarter-wave retarder before entering the polarimeter.

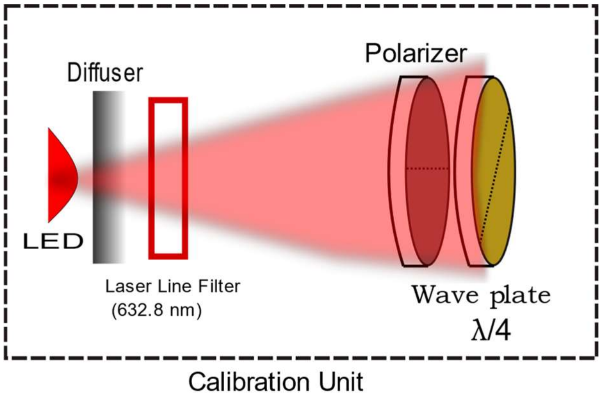

Fig. 5.2.1. Diagram of the experimental set-up to illuminate the calibration samples.

Using combinations of the orientation of the polarizer and the quarter wave plate, the normalized Stokes vectors for the four ideal samples are:

$$\boldsymbol{S}_{(0,135)} = \begin{pmatrix} 1 \\ 0 \\ 0 \\ -1 \end{pmatrix}, \boldsymbol{S}_{(10,90)} = \begin{pmatrix} 1 \\ 0.9397 \\ 0 \\ 0.3420 \end{pmatrix}, \boldsymbol{S}_{(-50,30)} = \begin{pmatrix} 1 \\ -0.4698 \\ -0.8138 \\ 0.3420 \end{pmatrix}, \boldsymbol{S}_{(70,150)} = \begin{pmatrix} 1 \\ -0.4698 \\ 0.8138 \\ 0.3420 \end{pmatrix}, \tag{5.2.1}$$

where $\boldsymbol{S}_{(\theta_p,\theta_r)}$ represents the Stokes vector or the light passing through a linear polarizer with transmission axis at θ_p and a quarter wave plate with fast axis at θ_r. Considering an ideal polarimeter, and hence an ideal instrument matrix, we obtained an image for the degree of polarization and one image for each Stokes parameter $\boldsymbol{S}_1$, $\boldsymbol{S}_2$ and $\boldsymbol{S}_3$. The experimentally obtained images are shown in Fig. 5.2.2 to 5.2.5.

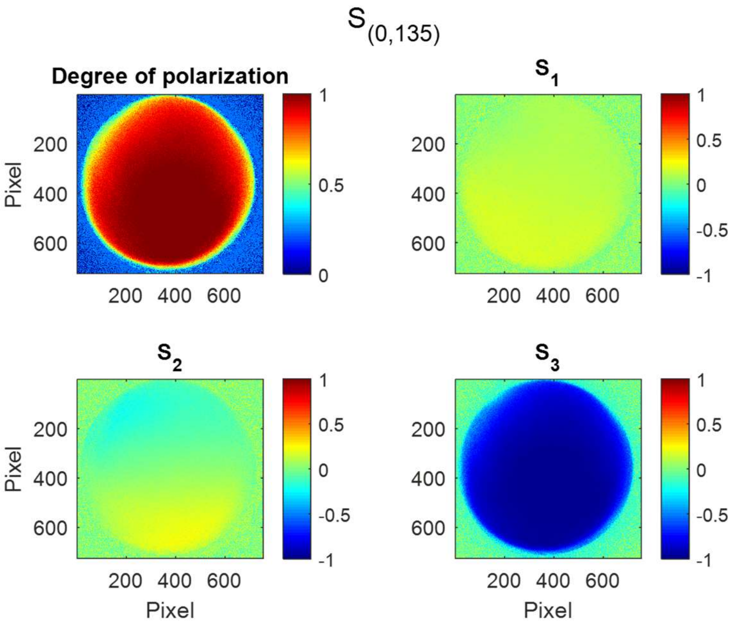

Fig. 5.2.2. Polarimetric images for $\boldsymbol{S}_{(0,135)}$ sample.

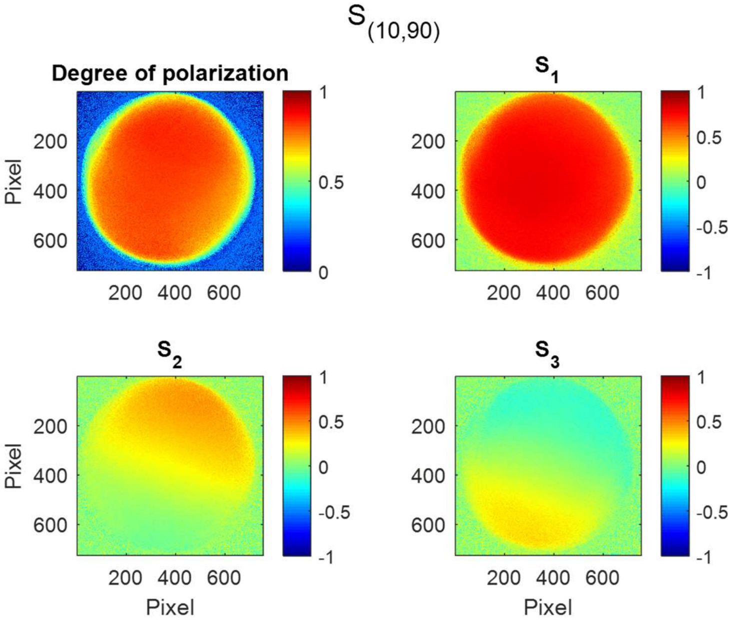

Fig. 5.2.3. Polarimetric images for $\boldsymbol{S}_{(10,90)}$ sample.

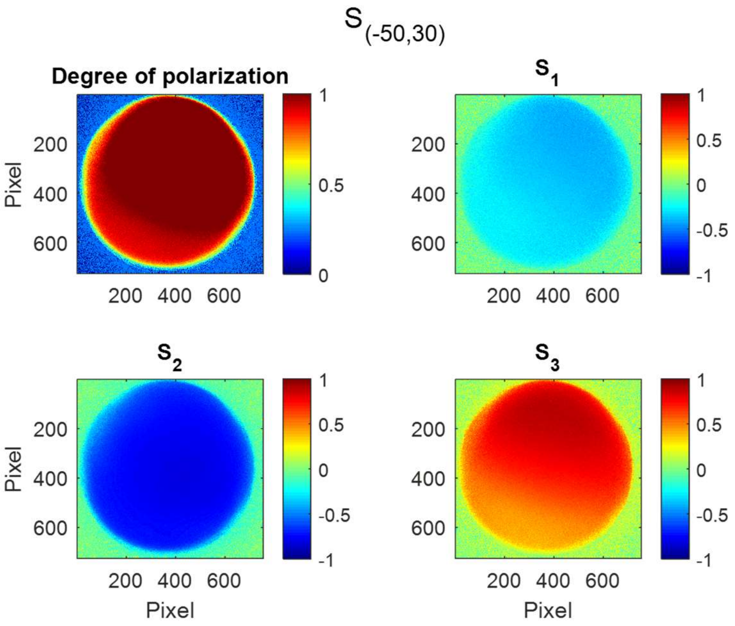

Fig. 5.2.4. Polarimetric images for $\boldsymbol{S}_{(-50,30)}$ sample.

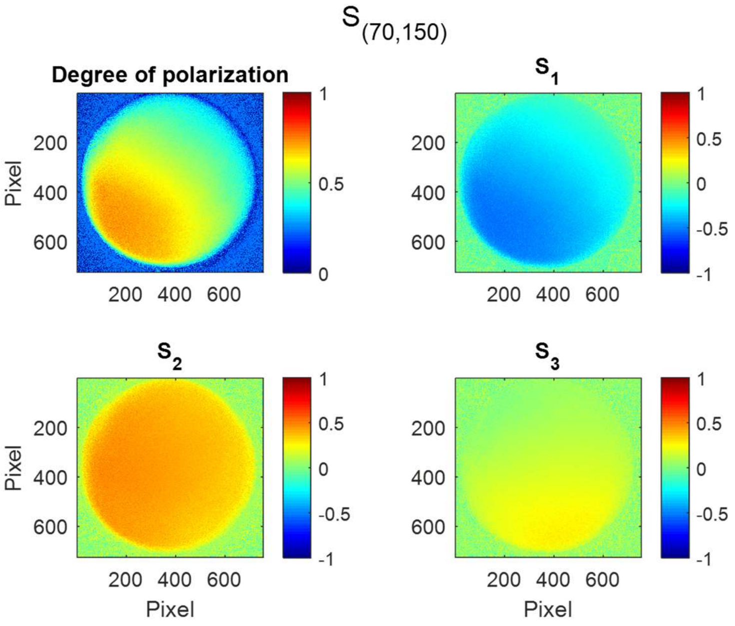

Fig. 5.2.5. Polarimetric images for $\boldsymbol{S}_{(70,150)}$ sample.

We calculated the mean value and standard deviation for each of the Stokes parameters and degree of polarization for each sample. The obtained values are presented in equations from 5.2.2 to 5.2.5,

$$\boldsymbol{S}_{(0,135)} = \begin{pmatrix} 1 \\ 0.11 \pm 0.04 \\ 0.01 \pm 0.12 \\ -0.95 \pm 0.07 \end{pmatrix}, DoP = 0.92 \pm 0.12; \tag{5.2.2}$$

$$\boldsymbol{S}_{(10,90)} = \begin{pmatrix} 1 \\ 0.73 \pm 0.04 \\ 0.20 \pm 0.14 \\ 0.05 \pm 0.15 \end{pmatrix}, DoP = 0.75 \pm 0.08; \tag{5.2.3}$$

$$\boldsymbol{S}_{(-5\ \ ,30)} = \begin{pmatrix} 1 \\ -0.35 \pm 0.05 \\ -0.76 \pm 0.05 \\ 0.67 \pm 0.15 \end{pmatrix}, DoP = 1.05 \pm 0.14; \tag{5.2.4}$$

$$\boldsymbol{S}_{(70,150)} = \begin{pmatrix} 1 \\ -0.39 \pm 0.10 \\ 0.40 \pm 0.04 \\ 0.14 \pm 0.07 \end{pmatrix}, DoP = 0.55 \pm 0.11. \tag{5.2.5}$$

As can be seen the results were not as we expected from the theoretical Stokes parameters. The degree of polarization differs from the theoretical value of one, in particular in $S_{(10,90)}$ and $S_{(70,150)}$, where the difference is more than a 25%. In the case of $\boldsymbol{S}_{(-50,30)}$, we obtained a value bigger than one, which lacks of physical meaning considering that the real irradiance measurements differ from the expected, due to differences between the experimental instrument matrix and the theoretical matrix. We can also see that the standard deviation of each parameter varies from one parameter to another, with no particular trend. The absolute error was calculated for each sample, $\Delta S_{(\theta_p,\theta_r)} = \left| S^{exp}_{(\theta_p,\theta_r)} - S^{theo}_{(\theta_p,\theta_r)} \right|$, and the total RMSE for all the samples. These values are presented in equation 5.2.6 and 5.2.7

$$\Delta S_{(0,135)} = \begin{pmatrix} 0 \\ 0.11 \\ 0.01 \\ 0.05 \end{pmatrix}; \Delta S_{(10,90)} = \begin{pmatrix} 0 \\ 0.21 \\ 0.20 \\ 0.29 \end{pmatrix}; \Delta S_{(-50,30)} = \begin{pmatrix} 0 \\ 0.12 \\ 0.05 \\ 0.33 \end{pmatrix}; \Delta S_{(70,150)} = \begin{pmatrix} 0 \\ 0.08 \\ 0.41 \\ 0.20 \end{pmatrix}, \tag{5.2.6}$$

$$RMSE = \left(\sum_{\mathrm{N}=1}^{3} \sum_{\mathrm{n}=1}^{4} \frac{1}{Nn} \left(S_N^{exp} - S_N^{theo} \right)^2{}_n \right)^{1/2} = 0.220. \tag{5.2.7}$$

In fact, the total RMSE is 37% larger than the results of the non-optimized polarimeter with four measurements presented in section 4.1. We tried to calibrate these results using the procedure shown in section 4.2, but the method failed. These results suggest that the polarimeter is not completely optimized. We decided to calibrate our polarimeter in each pixel of the image, considering ideal samples. For the set of incident Stokes vectors, used as calibration samples, we can put the vectors as the columns of a matrix $\overline{\boldsymbol{S}} = [\boldsymbol{S}_{sample-1}, \boldsymbol{S}_{sample-2}, \dots, \boldsymbol{S}_{sample-n}]$, and rewrite equation (2.2.2) to estimate the instrument matrix as,

$$\overline{\boldsymbol{A}} = \overline{\boldsymbol{IS}^{-1}}, \tag{5.2.8}$$

where $\overline{\boldsymbol{I}}$ is the [4 x n] matrix with the irradiance measurements for each of the n samples and the four polarimeter configurations. This way we can relate the irradiance measurements with an instrument matrix, and thus a condition number in each pixel of the camera. In equation 5.2.9 we present the mean value and standard deviation of the elements of the instrument matrix, also in Fig. 5.2.6 we present the condition number in every pixel of the calibrated polarimeter.

$$\overline{\boldsymbol{A}}_1 = 1/2\begin{pmatrix} 0.99 \pm 0.01 & 0.33 \pm 0.06 & 0.07 \pm 0.15 & -0.72 \pm 0.08 \\ 0.99 \pm 0.01 & -0.86 \pm 0.08 & -0.14 \pm 0.08 & 0.13 \pm 0.07 \\ 0.94 \pm 0.02 & 0.11 \pm 0.07 & 0.77 \pm 0.07 & -0.01 \pm 0.12 \\ 0.97 \pm 0.02 & -0.10 \pm 0.18 & -0.44 \pm 0.10 & 0.67 \pm 0.10 \end{pmatrix}, \tag{5.2.9}$$

In Fig. 5.2.6 theoretically we expected a condition number of 1.73 in all the pixels of the image, but as can be seen the optimization varies in the polarimeter, which is an undesirable effect that can be attributed to the variations over the aperture presented in the previous section. From this calibration we calculated the average and standard deviation of the condition number in the polarimeter, as well as the probabilities of obtaining a CN smaller than 2, which we consider a well optimized polarimeter, smaller than 2.59 which is considered a moderately optimized polarimeter, and the probabilities of obtaining a CN smaller than 3 which we considered a poorly optimized polarimeter. These results are shown in table 5.2.1.

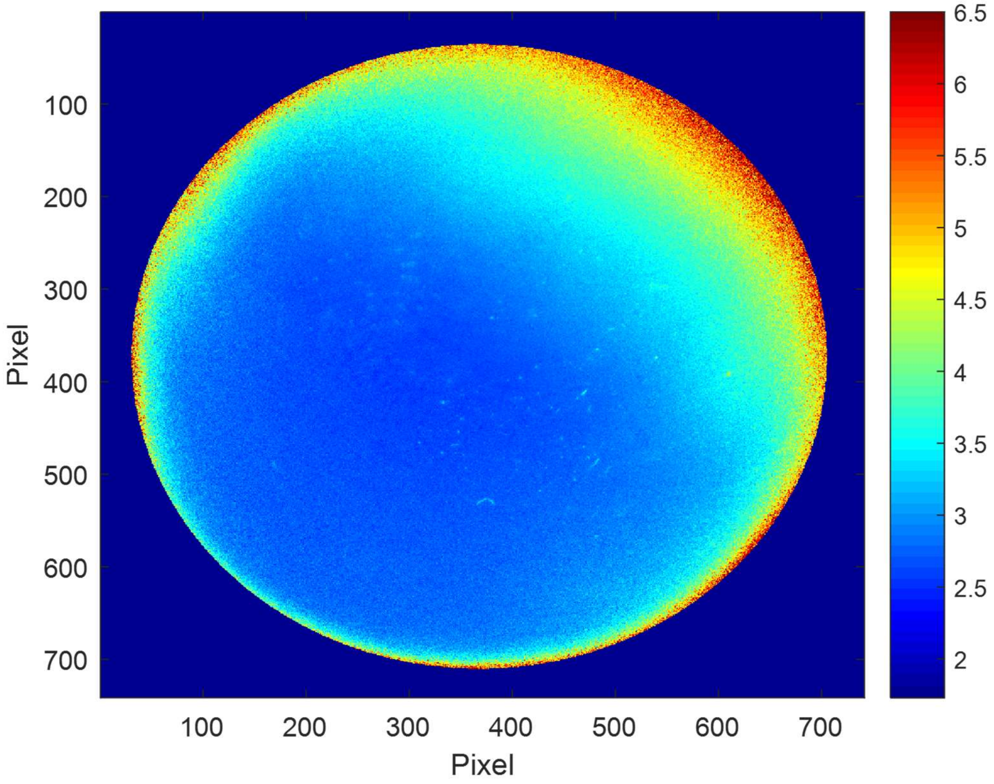

Fig. 5.2.6. Condition number of the calibrated polarimeter.

Calibrated polarimeter	Average	CN<2	CN<2.59	CN>3	Percentile 99
Calculated values	3.28 ± 0.74	0%	4%	49%	CN<5.7

Table 5.2.1. Results of the calibration of the polarimeter.

These results suggest that the variations of the retardance parameters over the LCVR aperture limit the application of these devices in imaging polarimeters. It can also be seen that the polarimeter has a different optimization in each pixel of the image, furthermore only a small percentage of the pixels are at least moderately optimized. The results in this section show that an optimization and a calibration are not sufficient to guarantee accurate polarimetric measurements and a model is necessary for the optimization of the polarimeter to reduce the effect of systematic error on the optimization of imaging polarimeters. This will be discussed in the next chapter, using numerical simulations.

6 Analysis of the effect of experimental errors on the optimization

As mentioned before, a model is required to optimize the polarimeter to reduce the effect of instrumental errors on the final measurements. As we have seen, the optical retardance introduced by these devices is in general not homogenous across the aperture, and the fast-axis orientation changes with the applied voltage. We have optimized the polarimeter in terms of the condition number, but the effects of LCVR variations are not considered, and a calibration is not enough. Although the polarimeter can be calibrated these errors can lead to a non-optimized polarimeter and to larger than expected noise amplification as shown in the Stokes imaging polarimeter in section 5.2.

In this chapter we analyze the impact of errors on LCVRs in a set of optimized Stokes polarimeters. In particular the effect of retardance and fast-axis orientation errors on a set of four differently optimized polarimeter schemes, previously published, based on two LCVRs. The set of Stokes polarimeters are simulated adding errors in the induced retardance and fast-axis orientation, as well as an error in the transmission axis of the polarizer. Then the CN is calculated to observe the effect of these errors on the optimization. We also present the propagation error theory to choose the best experimental parameters to reduce the nonideal effects in optimized polarimeters. The objective is to find a four-measurement scheme optimized but less sensitive to systematic errors. The instrument matrix and CN of the analyzed polarimeter schemes, with the minimum number of measurements (four), are:

$$\bar{\boldsymbol{A}}_{\boldsymbol{1}} = \begin{pmatrix} \bar{\boldsymbol{M}}_{pol}\bar{\boldsymbol{M}}_{R2}(27.4°, 315°)\bar{\boldsymbol{M}}_{R1}(72.4°, 135°) \\ \bar{\boldsymbol{M}}_{pol}\bar{\boldsymbol{M}}_{R2}(27.4°, 135°)\bar{\boldsymbol{M}}_{R1}(72.4°, 135°) \\ \bar{\boldsymbol{M}}_{pol}\bar{\boldsymbol{M}}_{R2}(27.4°, 135°)\bar{\boldsymbol{M}}_{R1}(72.4°, 315°) \\ \bar{\boldsymbol{M}}_{pol}\bar{\boldsymbol{M}}_{R2}(27.4°, 315°)\bar{\boldsymbol{M}}_{R1}(72.4°, 315°) \end{pmatrix}$$

$$= \frac{1}{2}\begin{pmatrix} 1 & 0.47 & -0.33 & -0.82 \\ 1 & -0.94 & -0.33 & 0.00 \\ 1 & 0.00 & 1.00 & 0.00 \\ 1 & 0.47 & -0.33 & 0.82 \end{pmatrix} : \mathrm{CN} = 1.735, \tag{6.0.1}$$

$$\bar{\boldsymbol{A}}_{\boldsymbol{2}} = \begin{pmatrix} \bar{\boldsymbol{M}}_{pol}\bar{\boldsymbol{M}}_{R2}(62.64°, 45°)\bar{\boldsymbol{M}}_{R1}(17.64°, 45°) \\ \bar{\boldsymbol{M}}_{pol}\bar{\boldsymbol{M}}_{R2}(62.64°, 225°)\bar{\boldsymbol{M}}_{R1}(17.64°, 45°) \\ \bar{\boldsymbol{M}}_{pol}\bar{\boldsymbol{M}}_{R2}(62.64°, 45°)\bar{\boldsymbol{M}}_{R1}(17.64°, 225°) \\ \bar{\boldsymbol{M}}_{pol}\bar{\boldsymbol{M}}_{R2}(62.64°, 225°)\bar{\boldsymbol{M}}_{R1}(17.64°, 225°) \end{pmatrix}$$

$$= \frac{1}{2}\begin{pmatrix} 1 & 0.47 & 0.33 & -0.82 \\ 1 & -0.94 & 0.33 & 0.00 \\ 1 & 0.00 & -1.00 & 0.00 \\ 1 & 0.47 & 0.33 & 0.82 \end{pmatrix} : \mathrm{CN} = 1.732, \tag{6.0.2}$$

$$\bar{\boldsymbol{A}}_{\boldsymbol{3}} = \begin{pmatrix} \bar{\boldsymbol{M}}_{pol}\bar{\boldsymbol{M}}_{R2}(45°, -16.3°)\bar{\boldsymbol{M}}_{R1}(22.5°, -3.59°) \\ \bar{\boldsymbol{M}}_{pol}\bar{\boldsymbol{M}}_{R2}(45°, 134°)\bar{\boldsymbol{M}}_{R1}(22.5°, -61.1°) \\ \bar{\boldsymbol{M}}_{pol}\bar{\boldsymbol{M}}_{R2}(45°, 49.3°)\bar{\boldsymbol{M}}_{R1}(22.5°, 103°) \\ \bar{\boldsymbol{M}}_{pol}\bar{\boldsymbol{M}}_{R2}(45°, 156°)\bar{\boldsymbol{M}}_{R1}(22.5°, 107°) \end{pmatrix}$$

$$= \frac{1}{2}\begin{pmatrix} 1 & 0.95 & 0.01 & 0.32 \\ 1 & -0.07 & -0.62 & -0.78 \\ 1 & -0.27 & 0.92 & -0.28 \\ 1 & -0.60 & -0.31 & 0.74 \end{pmatrix} : \mathrm{CN} = 1.738, \tag{6.0.3}$$

$$\bar{\boldsymbol{A}}_{\boldsymbol{4}} = \begin{pmatrix} \bar{\boldsymbol{M}}_{pol}\bar{\boldsymbol{M}}_{R2}(45°, 234.74°)\bar{\boldsymbol{M}}_{R1}(0°, 225°) \\ \bar{\boldsymbol{M}}_{pol}\bar{\boldsymbol{M}}_{R2}(45°, 125.26°)\bar{\boldsymbol{M}}_{R1}(0°, 225°) \\ \bar{\boldsymbol{M}}_{pol}\bar{\boldsymbol{M}}_{R2}(45°, 54.74°)\bar{\boldsymbol{M}}_{R1}(0°, 315°) \\ \bar{\boldsymbol{M}}_{pol}\bar{\boldsymbol{M}}_{R2}(45°, 305.26°)\bar{\boldsymbol{M}}_{R1}(0°, 315°) \end{pmatrix}$$

$$= \frac{1}{2}\begin{pmatrix} 1 & -0.58 & 0.58 & -0.58 \\ 1 & -0.58 & -0.58 & 0.58 \\ 1 & 0.58 & -0.58 & -0.58 \\ 1 & 0.58 & 0.58 & 0.58 \end{pmatrix} : \mathrm{CN} = 1.732. \tag{6.0.4}$$

As we can see in all cases the polarimeters are optimized, having a CN equal to or very close to the minimum. The configuration represented by $\bar{\boldsymbol{A}}_{\boldsymbol{1}}$ was found and used by De Martino et al. [34], also used in the polarimeter presented in section 5.2. $\bar{\boldsymbol{A}}_{\boldsymbol{2}}$ was optimized, by us, following the same procedure. The polarimeter represented by $\bar{\boldsymbol{A}}_{\boldsymbol{3}}$ was discussed by Tyo [37], while $\bar{\boldsymbol{A}}_{\boldsymbol{4}}$ was found by maximizing the polarimetric efficiencies [38] and used by Alvarez-Herrero et al. [16].

6.1 Individual errors

For this analysis we calculated the CN obtained considering simulated individual misalignment errors in both LCVRs, as well as individual errors in the induced retardances. The error parameters are considered for a range from -20° to +20° in the induced retardance and from -15° to +15° in the axis position, which are larger than the errors presented in table 5.1.2, to have a clearer view of the behavior of the polarimeters. The results are shown Fig. 6.1.1, where the CN as a function of each error is plotted, and each parameter is represented by a different marker. In these graphs, θ_i represents the error in the axis position of the i-th LCVR, and δ_i represents the error in the retardance used in the i-th LCVR.

It can be observed that the errors in the axis positions (circle and cross marks), orange and blue lines, cause larger changes in the CN than the errors in the retardance values. This is because an error in the axis position will change the four rows of the instrument matrix, while an error in one retardance value will change one or maximum two rows of the instrument matrix. In the four configurations analyzed, the error parameter that has the biggest impact in the optimization is the error in fast-axis position of the second LCVR. It can also be seen that the direction of the error is important, this difference is evident in the first two configurations, but not in the case of $\bar{\boldsymbol{A}}_{\boldsymbol{4}}$, where the red line is symmetric. In Table 6.1.1 we show the maximum CN obtained in these results, for each error parameter.

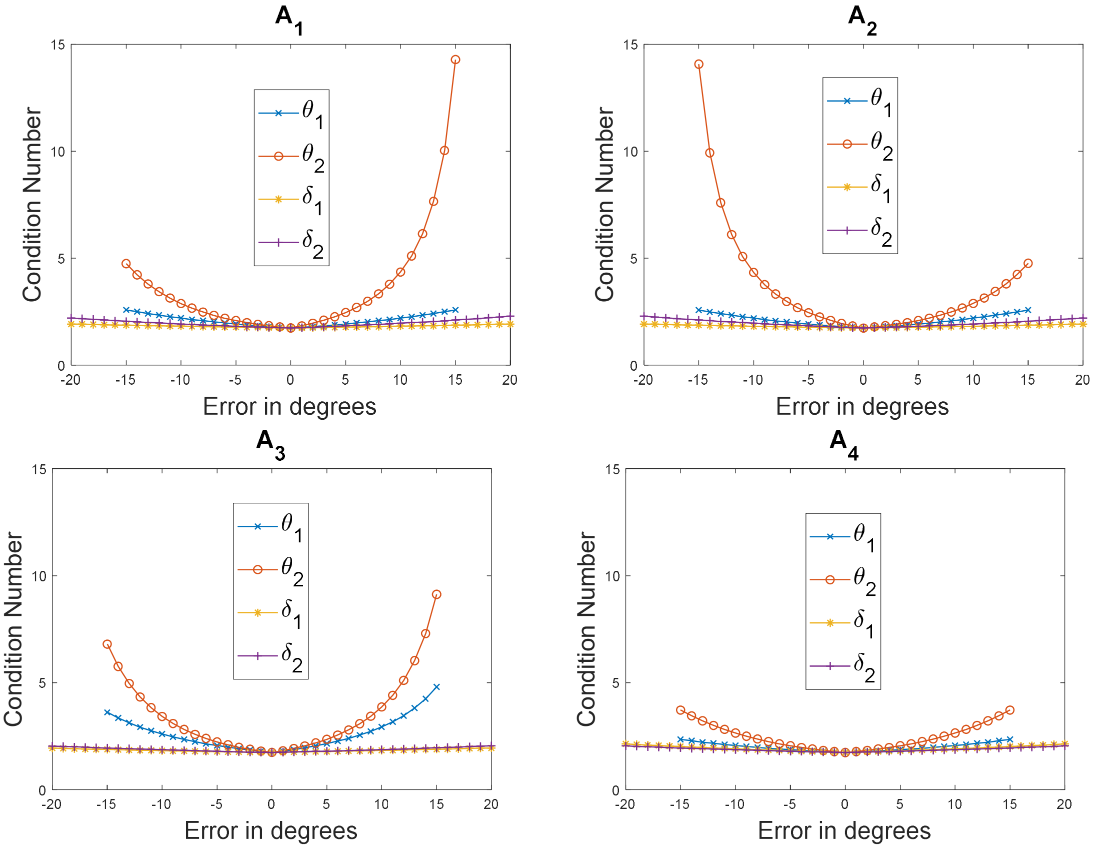

Fig 6.1.1. CN as a function of the errors, for each instrument matrix.

Polarimeter configuration	Error of ±15° in $\boldsymbol{\theta_1}$	Error of ±15° in $\boldsymbol{\theta_2}$	Error of ±20° in $\boldsymbol{\delta_{1,j}}$	Error of ±20° in $\boldsymbol{\delta_{2,j}}$
$\boldsymbol{\bar{A}_1}$	2.58	14.28	1.92	2.28
$\boldsymbol{\bar{A}_2}$	2.57	14.07	1.91	2.28
$\boldsymbol{\bar{A}_3}$	4.79	9.12	1.94	2.05
$\boldsymbol{\bar{A}_4}$	2.35	3.71	2.13	2.04

Table 6.1.1. Maximum CN obtained in each polarimeter with errors in the fast-axis position and retardance.

It is evident from table 6.1.1 that the parameters that contribute the most to the increase in the condition number are the axis positions of the LCVRs, in particular in the second retarder. The polarimeter represented by $\boldsymbol{\bar{A}_4}$ has the lowest values of the CN obtained with axis position errors. The configurations represented by $\boldsymbol{\bar{A}_1}$ and $\boldsymbol{\bar{A}_2}$ suffer the largest effect in the CN with errors in the second LCVR. We can also see that the polarimeter that suffers the largest impact of the errors in the fast-axis of the first LCVR is $\bar{A}_3$.

6.2 Simultaneous errors

Considering that the fast-axis position of the LCVRs has the biggest impact in the optimization, we calculated the CN with combinations of these errors in both retarders. In Fig. 6.2.1 we show the maps of the CN, with an upper bound of 3.46, which represents an increase of 100% from the ideal value. Each color line is an increase of approximately 0.22 in the CN. The upper bound was set considering te results presented in chapter 4, where we showed that using a polarimeter with a CN=3.22, the obtained results differ significantly from the expected values. Thus, we considering that using CN values above 3.46 are not useful for polarimetric measurements, as they will lead to inaccurate results.

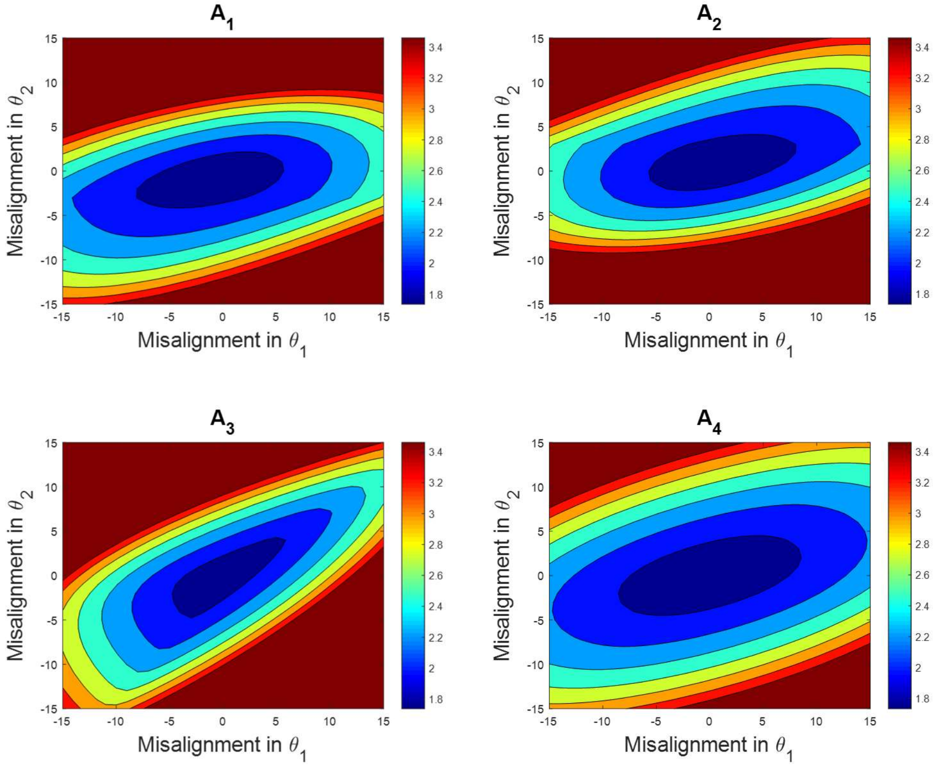

Fig. 6.2.1. CN maps as a function of error in the orientation of the LCVRs

In Fig. 6.2.1, we can see how the CN increases from the center, when there are no errors, to the maximum value considered, 3.46. In all configurations we can see in the bottom left corner and upper right corner, where the errors of both LCVRs are in the same direction and maintain the relative difference between retarders, tend to have a smaller CN, than in the opposite corners where the errors are in different directions, and the relative difference changes.

For the analysis of simultaneous retardance and axis position errors we simulated one million cases, adding random errors from a gaussian distribution of each error parameter to the LCVR configuration of the polarimeter. As presented in section 5.1, we measured the retardance variations in the aperture of the LCVRs, and the variations in the axis position as a function of the applied voltages. Using the results obtained in table 5.1.2, we decided to add errors of $\pm 9°$ in the retardance values, and $\pm 4°$ in the axis position of the LCVRs. We also considered an error of $\pm\ 1°$ in the axis position of the polarizer. We calculated the CN values for each one of the million cases and the Mean Absolute Error (MAE). In Fig. 6.2.2 we show the CN as a function of the MAE in each case and for every polarimeter scheme. The obtained values for the matrices $\overline{\boldsymbol{A}}_{\boldsymbol{1}}$ and $\overline{\boldsymbol{A}}_{\boldsymbol{2}}$, are shown in color green and red, but the results are very similar and are overlapped. The results for $\overline{\boldsymbol{A}}_{\boldsymbol{3}}$ are shown in blue, and for $\overline{\boldsymbol{A}}_{\boldsymbol{4}}$ are shown in cyan.

Fig. 6.2.2 shows the different behavior for each configuration, this difference is more evident when we have MAE values above 0.05. In particular, using $\overline{\boldsymbol{A}}_{\boldsymbol{4}}$, the CN tends to have smaller values, independently of the MAE, and using $\overline{\boldsymbol{A}}_{\boldsymbol{3}}$, tends to have larger values, with an increasing MAE. From these simulations, in the second column of table 6.2.1, we calculated the CN values for each case and the probabilities of obtaining a CN smaller than 2, which, from our experience, will represent the probabilities of having a well-optimized polarimeter. In the third column, we calculated values larger than 2.59, which represent the probabilities of having a poorly-optimized system, with an increment of 50% from the ideal value. Any value between 2 and 2.59 will be considered as a moderately-optimized polarimeter.

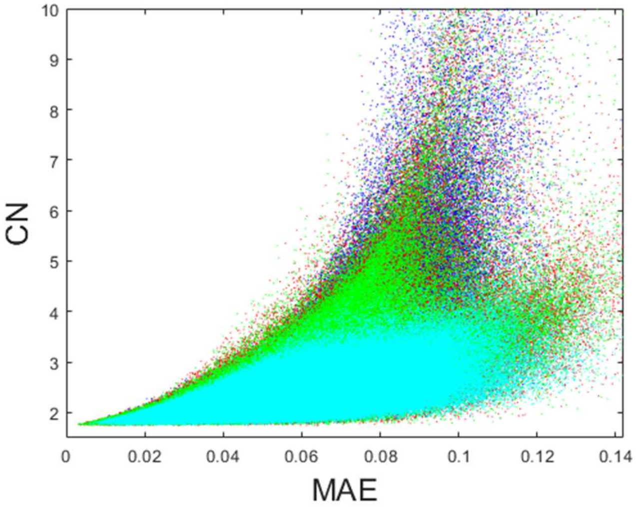

Fig. 6.2.2. CN maps as a function of the MAE in each polarimeter configuration. $\overline{\boldsymbol{A}}_{\boldsymbol{1}}$(green), $\overline{\boldsymbol{A}}_{\boldsymbol{2}}$(red), $\overline{\boldsymbol{A}}_{\boldsymbol{3}}$(blue) and $\overline{\boldsymbol{A}}_{\boldsymbol{4}}$(cyan)

Instrument Matrix	CN<2	CN>2.59	99 percentile
$\overline{\boldsymbol{A}}_{\boldsymbol{1}}$	16.2%	22.0%	CN<4.83
$\overline{\boldsymbol{A}}_{\boldsymbol{2}}$	16.3%	21.8%	CN<4.73
$\overline{\boldsymbol{A}}_{\boldsymbol{3}}$	10.9%	28.3%	CN<5.53
$\overline{\boldsymbol{A}}_{\boldsymbol{4}}$	17.4%	11.6%	CN<3.33

Table 6.2.1. Probabilities of obtaining a value of the CN in a given range for each polarimeter configuration with errors.

As can be seen from table 6.2.1, the probabilities of obtaining given values of the CN differ from one configuration to another, which means that the errors in the LCVRs have a different impact on the CN of the different polarimeters. The only configurations that have similar values are $\overline{\boldsymbol{A}}_{\boldsymbol{1}}$ and $\overline{\boldsymbol{A}}_{\boldsymbol{2}}$, but it should be noted that these configurations have similar instrument matrices, with only changes of sign. It can also be seen that the configuration represented by $\overline{\boldsymbol{A}}_{\boldsymbol{4}}$ has the minimum probability of obtaining larger values of the CN by a considerable difference compared to the other three configurations. This means $\bar{\boldsymbol{A}}_{\boldsymbol{4}}$ has the maximum probability of obtaining at least a moderately-optimized system. Also, the percentile 99 is presented, and a very significant difference is also found between polarimeters for this parameter. All the configurations except $\bar{\boldsymbol{A}}_{\boldsymbol{4}}$ have a limit larger than 4.73. This means that the configuration $\bar{\boldsymbol{A}}_{\boldsymbol{4}}$ is more stable in the presence of experimental errors than the other configurations. The configurations $\bar{\boldsymbol{A}}_{\boldsymbol{1}}$ and $\bar{\boldsymbol{A}}_{\boldsymbol{2}}$, have a better global performance than $\bar{\boldsymbol{A}}_{\boldsymbol{3}}$ because the sensitivity to the errors in the fast axis of the first LCVR is significantly larger in $\bar{\boldsymbol{A}}_{\boldsymbol{3}}$. Also, the probability of a well optimized polarimeters is reduced significantly in $\bar{\boldsymbol{A}}_{\boldsymbol{3}}$.

In this section we presented the results of simulations of different configurations of optimized polarimeters using LCVRs. It was found that different configurations of optimized systems have very different tolerances to experimental errors in the LCVR fast-axes positions. In particular, we identified a configuration, denominated $\bar{\boldsymbol{A}}_{\boldsymbol{4}}$ in this chapter, with four measurements that has smaller increases of CN with increases in the experimental error and, therefore, is more stable in the presence of these errors. This configuration reduces the probability of obtaining a CN larger than 2.59 by at least half compared to the other configurations, for errors in the range of ±9° in the retardance values, and ±4° in the axis position of the LCVRs.

6.3 Optimal alignment

To reduce the impact of errors in the axis position, which have the biggest impact in the optimization, we analyzed the error propagation in each LCVR. Analyzing the second Stokes parameter, S_1'', of the beam emerging from the second LCVR, we have the following expression

$$S_1'' = [\cos^2(2\theta_2) + \cos(\delta_2)\sin^2(2\theta_2)]S_1' + \big[\big(1 - \cos(\delta_2)\big)\sin(2\theta_2)\cos(2\theta_2)\big]S_2' \\ -[\sin(\delta_2)\sin(2\theta_2)]S_3', \tag{3.2.3}$$

where S_i' are the incident Stokes parameters coming from the first LCVR. The total error in the parameter S_1'' due to the second LCVR is given by the propagation equation,

$$\sigma_{S_1''}^2 = \sigma_{\theta_2}^2 \left(\frac{\partial S_1''}{\partial \theta_2}\right)^2 + \sigma_{\delta_2}^2 \left(\frac{\partial S_1''}{\partial \delta_2}\right)^2. \tag{6.3.1}$$

The retardance values will depend on the measured polarization state and we have seen in Fig. 6.1.1 that this error has a small impact in the change of the condition number so this term will not considered here. Then

$$\frac{\partial S_1''}{\partial \theta_2} = [2(\cos(\delta_2) - 1)\sin(4\theta_2)]S_1' - [2(\cos(\delta_2) - 1)\cos(4\theta_2)]S_2'$$

$$-[2\sin(\delta_2)\cos(2\theta_2)]S_3'. \tag{6.3.2}$$

In order to reduce the total contribution of the axis position of the second LCVR we need to reduce each of the terms on the right-hand side of equation (6.3.3). The terms depending on θ_2 are $\sin(4\theta_2)$, $\cos(4\theta_2)$, and $\cos(2\theta_2)$. To reduce the contributions to the total error, these terms should be zero, but we can only do this in a maximum of two of the three terms, using a fast-axis orientation of $\frac{(2n+1)\pi}{4} rad$, where n is an integer, since $\sin(4\theta_2) = 0$ and $\cos(2\theta_2) = 0$. This is consistent with the results presented in table 6.1.1 where the configurations with the lowest values of CN with errors in θ_2 are $\bar{\boldsymbol{A}}_{\mathbf{3}}$ and $\bar{\boldsymbol{A}}_{\mathbf{4}}$ and both of these configurations use $\theta_2 = 45°$. It can also be seen that the configurations $\bar{\boldsymbol{A}}_{\mathbf{1}}$ and $\bar{\boldsymbol{A}}_{\mathbf{2}}$ which use values of 27.4° and 64.64°, respectively, differ less than 5° to the values were the contribution in S_1' is maximum, this is 22.5° and 67.5°.

For the first LCVR all three Stokes parameters emerging from the first LCVR can contribute to the detected irradiance. With a similar analysis as that presented for the second LCVR we have

$$\frac{\partial S_1'}{\partial \theta_1} = [2(\cos(\delta_1) - 1)\sin(4\theta_1)]S_1^{inc} - [2(\cos(\delta_1) - 1)\cos(4\theta_1)]S_2^{inc} -$$

$$[2\sin(\delta_1)\cos(2\theta_1)]S_3^{inc}, \tag{6.3.3}$$

$$\frac{\partial S_2'}{\partial \theta_1} = [2(\cos(\delta_1) - 1)\cos(4\theta_1)]S_1^{inc} - [2(\cos(\delta_1) - 1)\sin(4\theta_1)]S_2^{inc} + [2\sin(\delta_1)\sin(2\theta_1)]S_3^{inc}, \tag{6.3.4}$$

$$\frac{\partial S_3'}{\partial \theta_1} = [2\sin(\delta_1)\cos(2\theta_1)]S_1^{inc} + [2\sin(\delta_1)\sin(2\theta_1)]S_2^{inc}. \tag{6.3.5}$$

The terms to be minimized are $\cos(2\theta_1)$ and $\sin(2\theta_1)$. Given that the two LCVRs cannot be at the same angle to produce all the required polarization states before passing through the polarizer, the term $\sin(2\theta_1)$ suggests the use of a fast- axis orientation of $\frac{n\pi}{2}\ rad$. This is also consistent with the values presented in table 6.1.1 where the configuration with the lowest contribution is $\bar{\boldsymbol{A}}_4$ which uses an orientation of $\theta_1 = 0°$. We can also see that the configuration $\bar{\boldsymbol{A}}_3$ which has the largest change in the CN with respect to θ_1, uses a value of 22.5° where the contribution to S_1' is maximum. We recommend to avoid using positions near 22.5° or 67.5°, in both LCVRs.

As mentioned above if we use an orientation of $45°$ in both retarders, which also reduces the error propagation in the first retarder, we cannot have an optimized set of measurements. This is because all the possible polarization states analyzed lie on a circumference where the Stokes parameter S_2 is always zero. This can be seen in Fig. 6.3.1, were all the possible polarization states analyzed, using both LCVRS at $45°$, and different retardance value combinations are plotted as a black line.

Another important benefit of using the LCVRs in the suggested optimal orientations, $\theta_1 = 0°$ and $\theta_2 = 45°$, as in $\bar{\boldsymbol{A}}_4$, is that the polarimeter is capable of analyzing any Stokes vector on the surface of the Poincaré sphere, unlike the other three cases $\bar{\boldsymbol{A}}_1$, $\bar{\boldsymbol{A}}_2$ and $\bar{\boldsymbol{A}}_3$, where the complete surface is not reachable. This can be seen in Fig. 6.3.2, where the black areas represent the Stokes vectors capable of being analyzed by each configuration. Considering that optimal configurations lead to a maximum volume tetrahedron inside the Poincare sphere, we represent the vertices of these ideal tetrahedrons with blue dots. When these vertices are deviated, due to errors, the limiting black area will also limit the volume of the figure inscribed in the

Poincare sphere. The capacity of the system to reach the complete Poincare sphere will help to maintain a bigger volume, and thus a smaller CN.

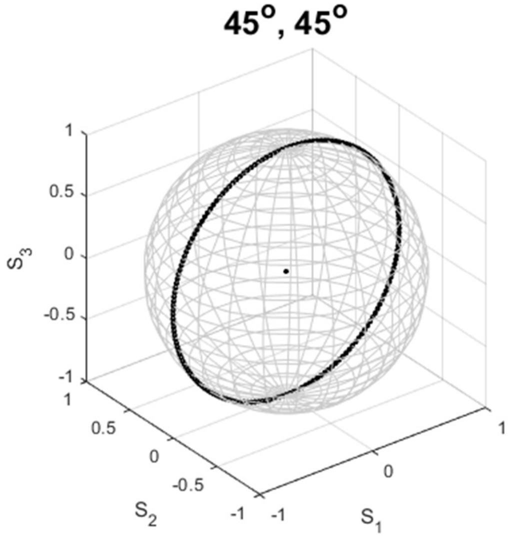

Fig. 6.3.1. Poincaré sphere areas able to be analyzed (black), by a polarimeter configuration with $\theta_1 = 45°$ and $\theta_2 = 45°$.

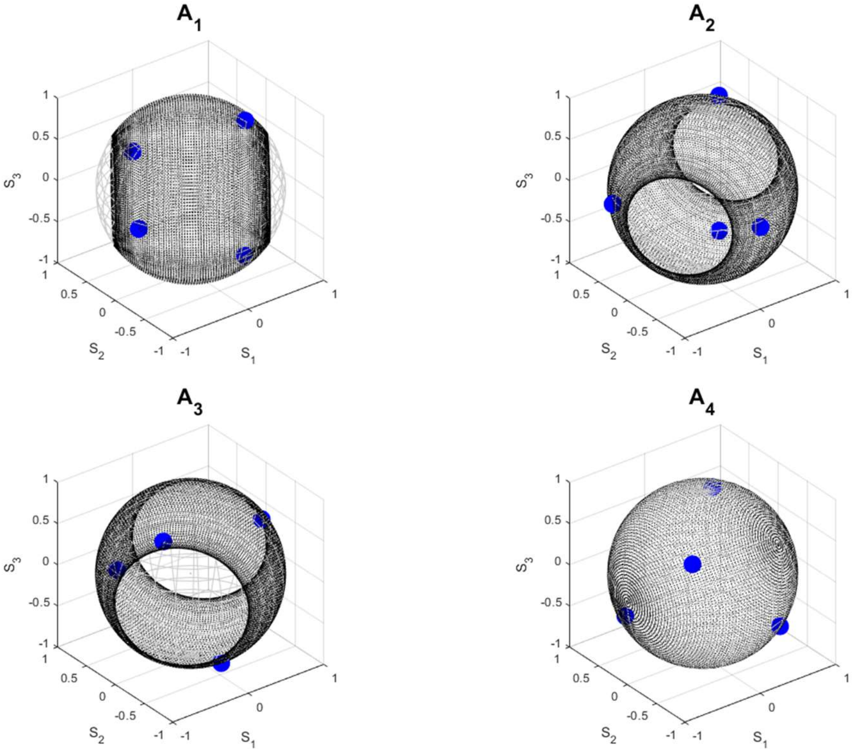

Fig. 6.3.2. Poincare sphere areas able to be analyzed (black), by each polarimeter configuration.

Moreover, using the proposed alignment, equation 3.2.3 reduces to

$$S_1'' = [\cos(\delta_2)]S_1' - [\sin(\delta_2)]S_3' \,. \tag{6.3.7}$$

In this case we do not have a contribution by S_2'. Thus, we do not have a contribution to the total error by this parameter of the first LCVR. Then, only two of the three Stokes parameters emerging from the first LCVR, equations (3.2.4) and (3.2.6), can contribute to the detected irradiance. Also, these equations are reduced to

$$S_1' = S_1^{inc}, \tag{6.3.8}$$

$$S_3' = -[\sin(\delta_1)]S_2^{inc} + [\cos(\delta_1)]S_3^{inc}. \tag{6.3.9}$$

In this case the contribution by different Stokes parameter is also reduced. And equation 3.2.7, which represents the measured irradiance reduces to,

$$I_{PSA} = S_0^{inc} + \cos\delta_2 S_1^{inc} + \sin\delta_1 \sin\delta_2 S_2^{inc} - \cos\delta_1 \sin\delta_2 S_3^{inc}. \tag{4.1.1}$$

This equation is easier to use, and the relation between the measured Stokes vectors and the retardance of each LCVR is very simple. In summary, we found that using a fast axis position for the second LCVR of 45° or 135°, and a fast axis position of 0° or 90° for the first LCVR, will lead to a more robust system that is less sensitive to experimental errors.

7 Conclusions

In this thesis we have shown the importance of considering instrumental errors in polarimeters based on LCVRs. The description of the properties and benefits of liquid crystals were presented, as well as the main problems when used in polarimetry. We find two main errors considering the nature of the liquid crystals: variations in the induced retardance and variations in the fast-axis position.

In addition to instrumental errors, we also considered noise in the irradiance measurement and showed experimentally the benefits of using an optimization of the Stokes polarimeter based on the CN, and the disadvantage of using a non-optimized system. However, the errors are higher than expected even with the optimization of the instrument matrix. To compensate the retardance and axis position errors, we have presented and verified a novel calibration method. The results show that this method can help reduce significantly the RMSE in polarimetric measurements, but only for optimized polarimeters. These results also confirm that it is important to consider an optimization, as well as a calibration.

A novel method to measure the spatial variations in the induced retardance was proposed. The method gives the complete information of the full aperture of the retarder with a simple and fast procedure. We also measured the variation of the fast-axis position with the applied voltage. With these results we obtained a better estimation of the voltages needed to induce a particular retardance value. We also estimated experimentally the magnitude of the two principal errors that will have an impact on the final measurements. The characterization method presented in this section showed a high spatial resolution, being able to detect small defects and variations in different points of the aperture.

The effect of these variations on a real imaging system was shown, implementing a Stokes imaging polarimeter and estimating the real instrument matrix. The experimental results showed the optimization differs from the ideal case, and the polarimeter has different condition numbers in each pixel of the image, furthermore only a small percentage of the pixels remained optimized. This demonstrates that even they are necessary, a condition number optimization of the instrument matrix and a calibration are not sufficient to guarantee accurate polarimetric measurements.

The results of the numerical simulations showed that different instrument matrices, even equally optimized, respond differently to instrumental errors. It was also found that the errors in the orientation of the second LCVR are more important than any other error parameter, as these errors have the biggest impact on the optimization metric. These results also suggest that the optimal alignment of the axis positions of the LCVRS in the design of polarimeters are $\frac{n\pi}{2}\,rad$, for the first retarder and $\frac{(2n+1)\pi}{4}rad$ for the second retarder. Using this alignment allows the polarimeter to measure any polarization state desired on the surface of the Poincaré sphere, producing a completely flexible system. Furthermore, the polarimeter is less sensitive to instrumental errors, producing an experimental design based on the reduction of the impact of instrumental errors in the final measurements.

Considering the principal errors in LCVRs, the results in this thesis showed the importance of using an optimal alignment, an optimization of the instrument matrix, and a calibration, in Stokes imaging polarimeters. Future work concerns deeper analysis of the optimization. Although we have proposed an optimal alignment and examined an optimization metric, if we minimize the CN or EWV, to optimize the instrument matrix, the solution will always be a tetrahedron inside the Poincaré sphere, regardless of the orientation or measured Stokes vectors, leading to infinite solutions. How to choose the best solution is not a trivial process. Further research is necessary, to have an accurate method to optimize the instrument matrix that helps differentiate one configuration from another.

References

[1] F. Liu, X. Shao and P. Han, "Desing of a circular polarization imager for contrast enhancement in rainy conditions," App. opt. **55**, (2016).

[2] J.S. Tyo, D.L. Goldstein, D.B. Chenault and J.A. Shaw, “Review of passive imaging polarimetry for remote sensing applications,” App. Opt. **45**(22), (2006).

[3] D. Miller and E. Dereniak, “Selective polarization imager for contrast enhacements in remote scattering media,” App. Opt. **51**, (2012).

[4] D. Louie, L. Tchvialeva, S. Kalia, H. Lui and T. Lee, “One-shot Stokes polarimetry for low-cost skin cancer detection,” Proc. of SPIE, 1086904-8, (2019).

[5] J. Zhou, H. He, Y. Wang and H. Ma, "Stage scoring of liver fibrosis using Mueller matrix microscope," Proc. of SPIE, 10024, (2017).

[6] A. Le Gratiet, M. Dubreuil, S. Rivet and Y. Le Grand, "Scanning mueller polarimetric microscopy," Opt. Lett. **41**, (2016).

[7] S. K. Solanki et al., "The polarimetric and helioseismic imager on solar orbiter," A&A, **642**, A11 (2020).

[8] C. Ejeta, H. Boehnhardt, S. Bagnulo, G. P. Tozzi, “Spectro-polarimetry of the bright side of Saturns moon lapetus,” A&A, **537**, A23 (2012).

[9] D. Goldstein, *Polarized Light* (CRC Press, Boca Raton, 2003).

[10] R.A. Chipman, *Handbook of Optics* (McGraw-Hill, 1995), Chapter 22.

[11] A. de Martino, Y-K- Kim, E. García-Caurel, B. Laude and B. Drévillon, “Optimized Mueller polarimeter with liquid crystals,” Opt. Lett. **28**(8), 616-618 (2003).

[12] A. Peinado, A. Lizana, J. Vidal, C. Iemmi, and J. Campos, “Optimization and performance criteria of a Stokes polarimeter based on two variable retarders,” Opt. Express **18**, 9815–9830 (2010).

[13] Y. Zhang, H. Zhao, P. Song, S. Shi, W. Xu, and X. Liang, "Ground-based full-sky imaging polarimeter based on liquid crystal variable retarders," Opt. Express **22**, 8749-8764 (2014).

[14] P. Terrier, J. M. Charbois, and V. Devlaminck, "Robust estimation of Stokes parameters with a partial liquid-crystal polarimeter under thermal drift," Appl. Opt. **53**, 6706-6712 (2014).

[15] W. A. Woźniak, P. Kurzynowski, and S. Drobczyński, "Adjustment method of an imaging Stokes polarimeter based on liquid crystal variable retarders," Appl. Opt. **50**, 203-212 (2011).

[16] A. Álvarez-Herrero, P. García Parejo, and M. Silva-López, "Fine tuning method for optimization of liquid crystal based polarimeters," Opt. Express **26**, 12038-12048 (2018).

[17] D. S. Sabatke, M. R. Descour, E. L. Dereniak, W. C. Sweatt, S. A. Kemme, and G. S. Phipps, “Optimization of retardance for a complete Stokes polarimeter,” Opt. Lett. **25**(11), 802–804 (2000).

[18] J. S. Tyo, “Design of optimal polarimeters: maximization of signal-to-noise ratio and minimization of systematic error,” Appl. Opt. **41**(4), 619–630 (2002).

[19] M. R. Foreman, F. Goudail, "On the equivalence of optimization metrics in Stokes polarimetry," Opt. Eng. **58**(8) 082410 (2019).

[20] I. Montes-González, N. C. Bruce, O. G. Rodríguez-Herrera, and O. Rodríguez Núñez, "Method to calibrate a full-Stokes polarimeter based on variable retarders," Appl. Opt. **58**, 5952-5957 (2019)

[21] C. N. Ramírez, I. Montes-González, N. C. Bruce, J. M. López-Téllez, O. G. Rodríguez-Herrera, and M. Rosete-Aguilar, "Characterization of retardance spatial variations over the aperture of liquid-crystal variable retarders," Appl. Opt. **60**, 2998-3005 (2021)

[22], I. Montes-González, and N. C. Bruce, "Error analysis of a Stokes imaging polarimeter based on liquid crystal variable retarders," Proc. SPIE **12184**, Ground-based and Airborne Instrumentation for Astronomy IX, 121846F (2022).

[23], I. Montes-González, M. Avendaño-Alejo, O. G. Rodríguez-Herrera, and N. C. Bruce, "Analysis of the effect of typical liquid-crystal retarder errors on optimized Stokes polarimeters," Paper in preparation (2022).

[24] Hecht, Eugene. Optics. Reading, Mass. :Addison-Wesley, 2002

[25] D. S. Sabatke, A. M. Locke, M. R. Descour, W. C. Sweatt, J. P. Garcia, E. L. Dereniak, S. A. Kemme, and G. S. Phipps, "Figures of merit for complete Stokes polarimeter optimization," Proceedings of SPIE, Vol. 4133 (2000).

[26] G.H. Golub, C. Reinsch,, "Singular value decomposition and least squares solutions," Numer. Math. 14, 403–420 (1970).

[27] R. Angst, "The condition of linear equations: alternative derivation," https://www2.math.ethz.ch/education/bachelor/lectures/hs2014/other/linalg_INFK/matrix-condition-number.pdf (November 1, 2022)

[28] M. R. Foreman, A. Favaro, and Andrea Aiello, "Optimal frames for polarization state reconstruction" Phys. Rev. Lett. **115**, 263901 (2015).

[29]. P. Garcia-Parejo, A. Campos-Jara, E. Garcia-Caurel, O. Arteaga, and A. Alvarez-Herrero. "Nonideal optical response of liquid cristal variable retarders and its impact on their performance as polarization modulators." Journal of Vacuum Scince & Technology **38**, 014009 (2020)

[30] P. Terrier, J. M. Charbois, and V. Devlaminck, "Fast-axis orientation dependence on driving voltage for a Stokes polarimeter based on concrete liquid-crystal variable retarders," Appl. Opt. **49**, 4278-4283 (2010).

[31] S. E. Gilman, T. G. Baur, D. J. Gallagher, N. K. Shankar, "Properties Of Tunable Nematic Liquid Crystal Retarders," Proc. SPIE 1166, Polarization Considerations for Optical Systems II, (1990).

[32] J. Vargas, N. Uribe-Patarroyo, J. A. Quiroga, A. Alvarez-Herrero, and T. Belenguer, "Optical inspection of liquid crystal variable retarder inhomogeneities," Appl. Opt. **49**, 568-574 (2010).

[33] W. H. Press, S. A. Teukolsky, W. T. Vetterling, and B. P. Flannery, Numerical Recipes in C, The Art of Scientific Computing (Cambridge University, 1992).

[34] A. De Martino, Y.-K. Kim, E. García-Caurel, B. Laude, and B. Drévillon, "Optimized Mueller polarimeter with liquid crystals," Opt. Lett. **28**(8), 616–618 (2003).

[35] https://www.thorlabs.com/newgrouppage9.cfm?objectgroup_id=8831&pn=LCC2415-VIS/M. (November 1, 2022)

[36] R. M. A. Azzam, I. M. Elminyawi, and A. M. El-Saba, "General analysis and optimization of the four-detector photopolarimeter," J. Opt. Soc. Am. A 5, 681-689 (1988).

[37] J. S. Tyo, "Noise equalization in Stokes parameter images obtained by use of variable-retardance polarimeters," Opt. Lett. **25**(16), (2000).

[38] M. Collados, "High-resolution spectropolarimetry and magnetometry," in Third Euroconference on Advances in Solar Physics: Magnetic Fields and Oscillations, B. Schmieder, A. Hofman, and J. Staude, eds., ASP Conf. Ser. 184, 3–22 ~Astronomical Society of the Pacific, San Francisco, 1999.

Acknowledgments

This work was funded by the Dirección General de Asuntos del Personal Académico (DGAPA) of the Universidad Nacional Autónoma de México (UNAM), through project PAPIIT IG100121. Ivan Montes-González thanks the Consejo Nacional de Ciencia y Tecnolgía (CONACyT), México for a doctoral grant.